Control Engineering Practice 21 (2013) 769–788

Contents lists available at SciVerse ScienceDirect

Control Engineering Practice

journal homepage: www.elsevier.com/locate/conengprac

Autonomous airship path following control: Theory and experiments

Zewei Zheng [a,b], Wei Huo [a,c,*], Zhe Wu [b]

[a] Science and Technology on Aircraft Control Laboratory, Beijing University of Aeronautics and Astronautics, Beijing 100191, PR China
[b] School of Aeronautic Science and Engineering, Beijing University of Aeronautics and Astronautics, Beijing 100191, PR China
[c] The Seventh Research Division, Beijing University of Aeronautics and Astronautics, Beijing 100191, PR China

ARTICLE INFO

Article history:
Received 22 April 2012
Accepted 4 February 2013
Available online 21 March 2013

Keywords:
Autonomous airship
Path following control
Trajectory linearisation control
Flight experiments

ABSTRACT

A novel path following control method related to the planar and spatial motions for an underactuated autonomous airship is presented. First, the trajectory linearisation control (TLC) theory is briefly described and the dynamic model of the airship is introduced. Then, based on the model, a path following strategy that integrates the guidance-based path following principle and the TLC theory is deduced. The designed control system possesses a cascaded structure composed of a guidance loop, an attitude kinematics loop and a dynamics control loop. Stability analysis shows that the controlled closed-loop system is asymptotically stable. Finally, experimental flight results for the airship following typical paths are illustrated to verify the effectiveness of the proposed approach.

1. Introduction

With the rapid progress of aerospace technologies, unmanned autonomous airships are considered to be a new platform for undertaking multiple tasks, including communication, surveillance, advertising, monitoring and inspection exploration. Airships, which can ideally hover above an area, present extended airborne capabilities for long duration studies, take-off and land vertically without the need for runway infrastructures, and have obvious advantages over the other unmanned aerial vehicles (UAV), such as airplanes and helicopters (Vasconcelos, Silvestre, Oliveira, & Guerreiro, 2010). Therefore, after 60 years of insignificance, the interest in airships has been revived. Many interesting projects are in progress (Acosta & Joshi, 2007; Bijker & Steyn, 2008; Frye, Gammon, & Qian, 2007; Lee, Lee, Won, & Bang, 2007; Moutinho & Azinheira, 2004; Xie, Luo, Rao, & Gong, 2007), especially projects regarding a stratospheric airship (high-altitude airship) (Jamison, Sommer, & Porche, 2005; Lee, Kim, & Yeom, 2006, 2009; Smith & Rainwater, 2003; Yoshikazu, Katsuya, & Kouichi, 2003), in which the stratospheric airship is used in place of satellites as a mobile, long-time and low-cost platform for communication.

Three types of flight control technologies play a key role in developing autonomous airships: stabilisation control, trajectory tracking control and path following control. For the stabilisation control of airships, linear control methods and a backstepping control approach have been used (Hygounenc & Soueres, 2002; Khoury & Gillett, 1999; Schmidt, 2007). However, because these controllers are based on the linearised model of airships, they are effective only around the equilibrium state. In addition, a dynamic inversion control method has been applied to the autonomous airship based on its nonlinear model (Acosta & Joshi, 2007; Moutinho & Azinheira, 2004). For trajectory tracking control, the backstepping technique has been applied to control an unmanned airship (Lee et al., 2007), which drives the position of the airship to approach a desired time-varying trajectory. Unlike the trajectory tracking control, the vehicle is required to reach and follow a path that is specified without temporal constraint in path following control research. Considering their low-manoeuvrability character, it is more suitable to study the path following control problem for airships. A backstepping design formulation of path following control for an underactuated autonomous airship has been deduced (Azinheira & Moutinho, 2008; Azinheira, Moutinho, & Paiva, 2009). A predefined path following controller for a robotic airship has been proposed based on computer vision-based navigation and fuzzy control strategy (Xie et al., 2007). Moreover, a path following controller for the AURORA airship has been designed by combining the H_∞ and PI control methods (Azinheira, Paiva, Ramos, & Bueno, 2000). However, most of the existing airship control methods, except rare ones such as Xie et al. (2007) and Miller, Sullivan, and McDonald (2007), are just verified by

* Corresponding author at: The Seventh Research Division, Beijing University of Aeronautics and Astronautics, Beijing 100191, PR China.
E-mail addresses: zeweizheng@buaa.edu.cn (Z. Zheng), weihuo@buaa.edu.cn (W. Huo), wuzhe@buaa.edu.cn (Z. Wu).

0967-0661/$ - see front matter © 2013 Elsevier Ltd. All rights reserved.
http://dx.doi.org/10.1016/j.conengprac.2013.02.002

simulations without any practical flight test. In this report, a feasible path following controller for an underactuated autonomous airship is developed and verified by practical flight experiments.

The control strategy introduced in this report integrates the guidance-based path following (GBPF) principle (Breivik & Fossen, 2005b) and the trajectory linearisation control (TLC) theory (Zhu, 1995, 1997). Before the GBPF principle was proposed, the path following problem was often solved in the error space expressed with the Serret–Frenet (SF) frame (Altafini, 2002; Samson, 1995). However, the kinematics in the SF frame contains a singularity point at the origin of the oscillating circle (Skjetne & Fossen, 2001). To avoid this, Breivik and Fossen (2004) presented the GBPF principle and proposed its example as controllers for marine surface vessels and autonomous underwater vehicles (Breivik & Fossen, 2005a). In the GBPF principle, an error relationship between a moving object and the path to be followed is established, and the path following problem is solved by driving the error to zero based on the Lyapunov stability theory. In addition, the TLC theory is a recently developed nonlinear tracking control strategy. It provides a robust stable control design without slow-varying constraints on the desired trajectories, interpolation of controller gains or trajectory dependent redesigns. The TLC theory is described as a nonlinear dynamic pseudo-inversion in the feedforward path, used with a linear, time-varying feedback controller to stabilise the linearised tracking error dynamics. Because compensation for the imperfect cancellation of the nonlinear system model is designed, the TLC may effectively handle the nonlinear time-varying residual dynamics better than the feedback linearisation control (Huang, Liu, & Zhu, 2009; Liu, Zhu, Williams, & Wu, 2008). Furthermore, it can be used in non-minimum phase systems (Mickle, Huang, & Zhu, 2004). Until now, the TLC theory has been successfully applied to reusable launch vehicle flight control (Zhu, Lawrence, & Fisher, 2002), omni-directional mobile robot control (Liu et al., 2008), tri-propeller vertical takeoff and landing UAV control (Huang et al., 2009), and quadrotor helicopter control (Zhu & Huo, 2010), among other applications.

In our path following control method, the GBPF principle is used to generate the desired attitude and the TLC theory is applied to track the attitude immediately. The designed control system possesses a cascaded structure composed of a guidance loop, an attitude kinematics loop and a dynamics control loop. The method is applicable for following all regularly parameterised paths, and the designed controller has no singularity point. Stability analysis shows that the closed-loop system controlled by this method is asymptotically stable. Furthermore, the controlled system possesses robustness for perturbations because of the inherited characteristics of the TLC theory. Experimental flight results for an autonomous airship following typical paths demonstrate the capability of the proposed method.

This report is organised as follows. Preliminaries of the TLC theory are introduced in Section 2. The airship mathematics model for controller design is presented in Section 3. In Section 4, the detailed process to design the path following controller is provided, and the stabilities of the closed-loop system and path following direction are analysed. Experimental flight results for attitude tracking, planar and spatial path following are given in Section 5. In the last section, a brief summary is concluded and future work is indicated.

2. Trajectory linearisation control theory

The TLC theory is mainly used to address the nonlinear system as follows:

$$\begin{cases} \dot{\xi}(t) = \boldsymbol{f}(\xi(t), \boldsymbol{v}(t), \boldsymbol{\theta}(t)), \\ \boldsymbol{\eta}(t) = \boldsymbol{h}(\xi(t), \boldsymbol{v}(t), \boldsymbol{\theta}(t)), \end{cases} \tag{1}$$

where $\xi(t) \in \mathbb{R}^n$, $\boldsymbol{v}(t) \in \mathbb{R}^l$ are states, inputs, outputs and parametric vectors, respectively. The purpose is to design a controller that enables $\boldsymbol{\eta}(t)$ to track command $\boldsymbol{\eta}_c(t)$ as precisely as possible.

In the TLC theory, the inversion of the nonlinear dynamic system is calculated based on its nominal model and a nominal control $\boldsymbol{v}_n(t)$ is then generated according to the command $\boldsymbol{\eta}_c(t)$. The system controlled by $\boldsymbol{v}_n(t)$ is denoted as $\dot{\xi}_c = \boldsymbol{f}(\xi_c, \boldsymbol{v}_n, \boldsymbol{\theta})$. Because the inversion is often an approximation, the command and practical variables may contain errors. The errors of states, inputs and outputs are defined as $\xi_e(t) = \xi(t) - \xi_c(t)$, $\boldsymbol{v}_e(t) = \boldsymbol{v}(t) - \boldsymbol{v}_n(t)$ and $\boldsymbol{\eta}_e(t) = \boldsymbol{\eta}(t) - \boldsymbol{\eta}_c(t)$, respectively. Then, the error dynamics of nonlinear tracking is available as follows:

$$\begin{cases} \dot{\xi}_e = \boldsymbol{f}(\xi_c + \xi_e, \boldsymbol{v}_n + \boldsymbol{v}_e, \boldsymbol{\theta}) - \boldsymbol{f}(\xi_c, \boldsymbol{v}_n, \boldsymbol{\theta}) \triangleq \boldsymbol{f}_e(\xi_e, \boldsymbol{v}_e, \boldsymbol{\theta}, \xi_c, \boldsymbol{v}_n), \\ \boldsymbol{\eta}_e = \boldsymbol{h}(\xi_c + \xi_e, \boldsymbol{v}_n + \boldsymbol{v}_e, \boldsymbol{\theta}) - \boldsymbol{h}(\xi_c, \boldsymbol{v}_n, \boldsymbol{\theta}) \triangleq \boldsymbol{h}_e(\xi_e, \boldsymbol{v}_e, \boldsymbol{\theta}, \xi_c, \boldsymbol{v}_n). \end{cases} \tag{2}$$

Linearising the above nonlinear tracking error equation (2) along the command trajectory gives the following linear time-varying system:

$$\begin{cases} \dot{\xi}_e = \boldsymbol{A}(t)\xi_e + \boldsymbol{B}(t)\boldsymbol{v}_e, \\ \boldsymbol{\eta}_e = \boldsymbol{C}(t)\xi_e + \boldsymbol{D}(t)\boldsymbol{v}_e, \end{cases} \tag{3}$$

where

$$\begin{aligned} \boldsymbol{A}(t) &= \left.\frac{\partial \boldsymbol{f}_e}{\partial \xi_e}\right|_{\xi_e = 0, \boldsymbol{v}_e = 0} = \left.\frac{\partial \boldsymbol{f}(\xi, \boldsymbol{v})}{\partial \xi}\right|_{\xi = \xi_c, \boldsymbol{v} = \boldsymbol{v}_n}, \\ \boldsymbol{B}(t) &= \left.\frac{\partial \boldsymbol{f}_e}{\partial \boldsymbol{v}_e}\right|_{\xi_e = 0, \boldsymbol{v}_e = 0} = \left.\frac{\partial \boldsymbol{f}(\xi, \boldsymbol{v})}{\partial \boldsymbol{v}}\right|_{\xi = \xi_c, \boldsymbol{v} = \boldsymbol{v}_n}, \\ \boldsymbol{C}(t) &= \left.\frac{\partial \boldsymbol{h}_e}{\partial \xi_e}\right|_{\xi_e = 0, \boldsymbol{v}_e = 0} = \left.\frac{\partial \boldsymbol{h}(\xi, \boldsymbol{v})}{\partial \xi}\right|_{\xi = \xi_c, \boldsymbol{v} = \boldsymbol{v}_n}, \\ \boldsymbol{D}(t) &= \left.\frac{\partial \boldsymbol{h}_e}{\partial \boldsymbol{v}_e}\right|_{\xi_e = 0, \boldsymbol{v}_e = 0} = \left.\frac{\partial \boldsymbol{h}(\xi, \boldsymbol{v})}{\partial \boldsymbol{v}}\right|_{\xi = \xi_c, \boldsymbol{v} = \boldsymbol{v}_n}. \end{aligned}$$

Therefore, the tracking control of the nonlinear system (1) can be solved by designing a stabilising controller for the linear time-varying system (3). The structure of the TLC theory is summarised in Fig. 1.

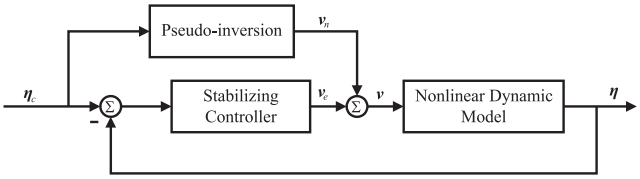

Fig. 1. Structure of the TLC theory.

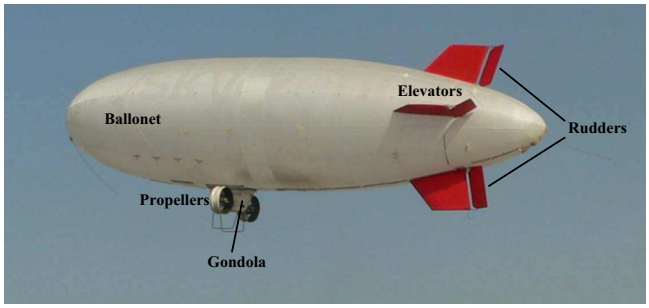

Fig. 2. Structure of the autonomous airship.

Because the derivative signals of the system model should be obtained from current and past states, the derivative of the exact inversion model needs future states of the system, which is impossible to implement. Therefore, a type of approximation called pseudo-inversion (Zhu & Huo, 2010) is introduced to replace the exact inversion. The pseudo-inversion is achieved using a second-order pseudo-differentiator with the following form:

$$\begin{cases} \dot{x}_1(t) = x_2(t), \\ \dot{x}_2(t) = -\omega_d^2(x_1(t)-\delta(t))-2\xi_d\omega_d x_2(t), \\ \sigma(t) = x_2(t), \end{cases} \tag{4}$$

where $\sigma(t)$ is regarded as the derivative of $\delta(t)$, ξ_d is fixed to 0.707 as the optimal damping ratio, and ω_d is the bandwidth. A larger value of the bandwidth contributes to a better approximation but greater high-frequency noise.

3. Modelling for airship

The airship (Fig. 2) considered here has a traditional ellipsoidal ballonet. Buoyancy is provided by helium contained in the ballonet. The flight control system, power system and payloads are equipped in a gondola fixed below the ballonet. The aerodynamic control surfaces, such as rudders and elevators, are attached to the empennage surfaces. The deflections of the rudders control the yaw movement, whereas the elevators influence the pitch rotations. The propellers are fixed on both sides of the gondola and are vectored thrust systems with rotation units about their horizontal axes. The propellers provide the main propulsive force for flight.

3.1. Reference frames

When considering the modelling of airplanes, the earth and body reference frames should be defined first. The earth reference frame (ERF) is fixed to the earth with its origin O_g located at a fixed point on the ground. The O_gx_g-axis points north, the O_gz_g-axis points to the earth core and the O_gy_g-axis points east. The body reference frame (BRF) is attached to the airship with its origin O coincident with the centre of volume (CV), as shown in Fig. 3. The Ox-axis points to the head of the airship. The Oz-axis is perpendicular to the Ox-axis and points downwards. The Oy-axis is determined by the right-hand rule and points towards the right.

The airship position and attitude of O_g are described in ERF by $\boldsymbol{\zeta} = [x,y,z]^T$ and $\boldsymbol{\gamma} = [\phi,\theta,\psi]^T$. The airship velocity and angular velocity of O_g are defined in BRF by $\upsilon = [u,v,w]^T$ and $\boldsymbol{\omega} = [p,q,r]^T$. The torques and products of inertia are described in BRF by $\{I_x,I_y,I_z\}$ and $\{I_{xy},I_{yz},I_{xz}\}$, respectively. Because the airframe is symmetric about the lateral plane, the products of inertia $I_{xy} = I_{yz} = 0$.

3.2. Force analysis

The airship depends on buoyancy to stay in the air, not lift, as traditional aircraft do; therefore, it has an enormous volume and moves slowly. Hence, the force analysis for the airship is not exactly the same as that for an airplane. The external forces applied to the airship include gravity, buoyancy, aerodynamic force, added inertia force and propulsive force. Here, the detailed expressions of these forces and torques except control force are not listed; these characteristics have been described previously (Mueller & Paluszek, 2004).

The practical actuators of the airship are shown in Fig. 3. It is obvious that the airship is underactuated because there are four independent actuators but six degrees of freedom of motion. Let δ_R indicate the deflections of the trailing edge flaps of the rudders and let δ_E indicate the deflections of the trailing edge flaps of the elevators. The influence of the rudders and elevators are represented in the aerodynamic forces and are written as $\boldsymbol{u}_\delta \triangleq [\delta_R,\delta_E]^T$. Propellers provide the force for moving. It is convenient to express the propulsive force and torque as $\boldsymbol{F}_T = [F_{T,x},0,F_{T,z}]^T$, $\boldsymbol{M}_T = [0,F_{T,x}z_t-F_{T,z}x_t,0]^T$, where $F_{T,x} = 2F_T\cos\mu$, $F_{T,z} = 2F_T\sin\mu$. F_T and μ denote the propulsive

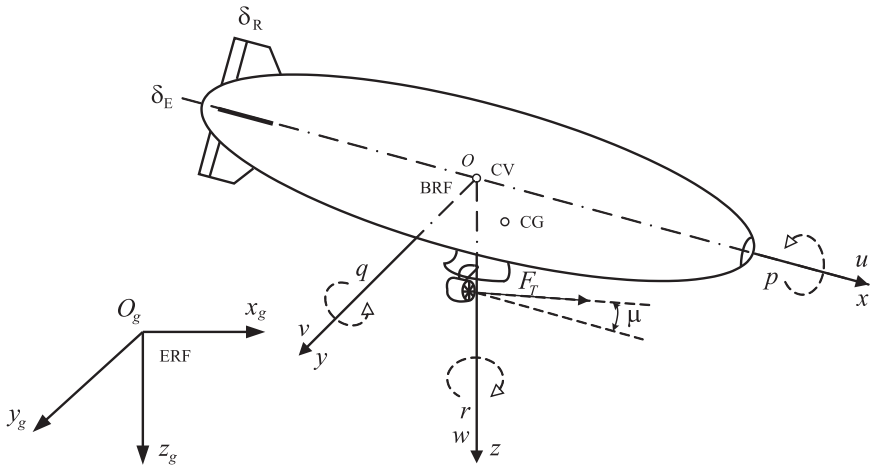

Fig. 3. Reference frames of the airship.

force and rotation angle of each propeller, respectively. $[x_t,y_t,z_t]^T$ is the position of the right propeller in the BRF and $[x_t,-y_t,z_t]^T$ is the position for the left one. The control vector provided by the propellers is defined as $\boldsymbol{u}_F \triangleq [F_{T,x},F_{T,z}]^T$.

3.3. Dynamic model of airship

To facilitate modelling of the airship, it is assumed that the airship forms a rigid body such that aeroelastic effects can be ignored (Moutinho & Azinheira, 2004). There has been considerable documentation on the detailed modelling process for an airship (Frye et al., 2007; Mueller & Paluszek, 2004; Schmidt, 2007). Therefore, the kinematical and dynamical equations are offered here directly.

3.3.1. Kinematical equations

The position kinematical equation is described as follows:

$$\dot{\boldsymbol{\zeta}} = \begin{bmatrix} \cos\theta\cos\psi & \sin\theta\cos\psi\sin\phi-\sin\psi\cos\phi & \sin\theta\cos\psi\cos\phi+\sin\psi\sin\phi \\ \cos\theta\sin\psi & \sin\theta\sin\psi\sin\phi+\cos\psi\cos\phi & \sin\theta\sin\psi\cos\phi-\cos\psi\sin\phi \\ -\sin\theta & \cos\theta\sin\phi & \cos\theta\cos\phi \end{bmatrix} \begin{bmatrix} u \\ v \\ w \end{bmatrix} \triangleq \boldsymbol{R}_g(\boldsymbol{\gamma})\boldsymbol{v}. \tag{5}$$

Additionally, the attitude kinematical equation is as follows:

$$\dot{\boldsymbol{\gamma}} = \begin{bmatrix} 1 & \tan\theta\sin\phi & \tan\theta\cos\phi \\ 0 & \cos\phi & -\sin\phi \\ 0 & \dfrac{\sin\phi}{\cos\theta} & \dfrac{\cos\phi}{\cos\theta} \end{bmatrix} \begin{bmatrix} p \\ q \\ r \end{bmatrix} \triangleq \boldsymbol{R}_\gamma(\boldsymbol{\gamma})\boldsymbol{\omega}. \tag{6}$$

3.3.2. Dynamical equations

The dynamical equation is described as follows:

$$\overline{\boldsymbol{A}} \begin{bmatrix} \dot{\boldsymbol{\omega}} \\ \dot{\boldsymbol{v}} \end{bmatrix} = \overline{\boldsymbol{N}} + \overline{\boldsymbol{B}} \begin{bmatrix} \boldsymbol{u}_F \\ \boldsymbol{u}_\delta \end{bmatrix}, \tag{7}$$

where

$$\overline{\boldsymbol{A}} = \begin{bmatrix} I_x & 0 & -I_{xz} & 0 & -mz_g & 0 \\ 0 & I_y+\rho\nabla k_3 & 0 & mz_g & 0 & -mx_g \\ -I_{xz} & 0 & I_z+\rho\nabla k_3 & 0 & mx_g & 0 \\ 0 & mz_g & 0 & m+\rho\nabla k_1 & 0 & 0 \\ -mz_g & 0 & mx_g & 0 & m+\rho\nabla k_2 & 0 \\ 0 & -mx_g & 0 & 0 & 0 & m+\rho\nabla k_2 \end{bmatrix},$$

$$\overline{\boldsymbol{N}} = \begin{bmatrix} -(I_z-I_y)qr+I_{xz}pq+mz_g(ur-wp)+L_a-z_gmg\cos\theta\sin\phi \\ -(I_x-I_z-\rho\nabla k_3)pr-I_{xz}(p^2-r^2)-mz_g(wq-vr)+mx_g(vp-uq)+M_a-z_gmg\sin\theta-x_gmg\cos\theta\cos\phi \\ -(I_y+\rho\nabla k_3-I_x)pq-I_{xz}qr-mx_g(ur-wp)+N_a+x_gmg\cos\theta\sin phi \\ -(m+\rho\nabla k_2)(wq-vr)+mx_g(q^2+r^2)-mz_gpr+X_a+(B-mg)\sin\theta \\ (m+\rho\nabla k_2)wp-(m+\rho\nabla k_1)ur-mx_gpq-mz_gqr+Y_a-(B-mg)\cos\theta\sin\phi \\ (m+\rho\nabla k_1)uq-(m+\rho\nabla k_2)vp-mx_grp+mz_g(q^2+p^2)+Z_a-(B-mg)\cos\theta\cos\phi \end{bmatrix},$$

$$\overline{\boldsymbol{B}}=\begin{bmatrix}0&0&0&0\\ z_t&-x_t&0&-QC_{m4}\\ 0&0&-QC_{n4}&0\\ 1&0&0&0\\ 0&0&QC_{y4}&0\\ 0&1&0&-QC_{z4}\end{bmatrix}.$$

In the above expressions, m is the mass of the airship; ∇ is the volume; $\{x_g,z_g\}$ are the x- and z-coordinates of the centre of gravity (CG); $\{k_1,k_2,k_3\}$ are the ellipsoid inertia factors for calculating the added mass and inertia matrices (Mueller & Paluszek, 2004); $Q=\rho V^2/2$ is the dynamic pressure, where ρ is the atmosphere density of flight altitude and $V=\sqrt{u^2+v^2+w^2}$ is the airspeed; C_{i4} $(i=m,n,y,z)$ are the aerodynamic coefficients (Mueller & Paluszek, 2004); and $\{X_a,Y_a,Z_a\}$ and $\{L_a,M_a,N_a\}$ are the aerodynamic forces and torques in the BRF, which have been represented in detail (Mueller & Paluszek, 2004, Eqs.(23)–(28)). For simplicity, it is assumed that the airship is always in neutral buoyant state, i.e., $mg\equiv B$, where g is the acceleration of gravity and B is the buoyancy that acts on the airship. Compared to the conventional aircraft model, the added mass is reflected on the mass issues of matrices $\overline{\boldsymbol{A}}$ and $\overline{\boldsymbol{N}}$ in (7), and the influence of CV modelling is such that $\overline{\boldsymbol{A}}$ is no longer a diagonal matrix that introduces the coupling of position and attitude dynamics states. For further reading, the reader can refer to the literature (Bennaceur & Azouz, 2012) for the influence of added mass and studies (Waishek, Dogan, & Bestaoui, 2009; Waishek, Kumar, Dogan, & Bestaoui, 2009)for the time varying mass effect on airship dynamics response and controller performance.

From (7), the position dynamical equation can be obtained as follows:

$$\begin{aligned}\dot{\upsilon}=&\begin{bmatrix}n_{u1}(vr-wq)+n_{u2}p^2+n_{u3}q^2+n_{u4}r^2+n_{u5}pr+n_{u6}pv+n_{u7}qu+n_{u8}M_a+n_{u9}X_a+n_{u10}Z_a\\ pw+n_{v1}ur+n_{v2}qr+n_{v3}pq+n_{v4}L_a+n_{v5}N_a+n_{v6}Y_a\\ -vp+n_{w1}uq+n_{w2}p^2+n_{w3}q^2+n_{w4}r^2+n_{w5}pr+n_{w6}(vr-wq)+n_{w7}M_a+n_{w8}X_a+n_{w9}Z_a\end{bmatrix}\\ &+\begin{bmatrix}n_{ug1}\sin\theta+n_{ug2}\cos\theta\cos\phi\\ n_{vg1}\cos\theta\sin\phi\\ n_{wg1}\sin\theta+n_{wg2}\cos\theta\cos\phi\end{bmatrix}+\begin{bmatrix}n_{u21}&n_{u22}&0&n_{u23}Q\\ 0&0&n_{u24}Q&0\\ n_{u25}&n_{u26}&0&n_{u27}Q\end{bmatrix}\begin{bmatrix}\boldsymbol{u}_F\\ \boldsymbol{u}_\delta\end{bmatrix}\triangleq\overline{\boldsymbol{N}}_\upsilon+\overline{\boldsymbol{G}}_\upsilon+\boldsymbol{u}_\upsilon,\end{aligned}\tag{8}$$

and the attitude dynamical equation is

$$\begin{aligned}\dot{\boldsymbol{\omega}}=&\begin{bmatrix}n_{p1}ur+n_{p2}wp+n_{p3}qr+n_{p4}pq+n_{p5}L_a+n_{p6}N_a+n_{p7}Y_a\\ n_{q1}(wq-vr)+n_{q2}pv+n_{q3}qu+n_{q4}p^2+n_{q5}q^2+n_{q6}r^2+n_{q7}pr+n_{q8}M_a+n_{q9}X_a+n_{q10}Z_a\\ n_{r1}ur+n_{r2}wp+n_{r3}qr+n_{r4}pq+n_{r5}L_a+n_{r6}N_a+n_{r7}Y_a\end{bmatrix}\\ &+\begin{bmatrix}n_{pg1}\cos\theta\sin\phi\\ n_{qg1}\sin\theta+n_{qg2}\cos\theta\cos\phi\\ n_{rg1}\cos\theta\sin\phi\end{bmatrix}+\begin{bmatrix}0&0&n_{u11}Q&0\\ n_{u12}&n_{u13}&0&n_{u14}Q\\ 0&0&n_{u15}Q&0\end{bmatrix}\begin{bmatrix}\boldsymbol{u}_F\\ \boldsymbol{u}_\delta\end{bmatrix}\triangleq\overline{\boldsymbol{N}}_\omega+\overline{\boldsymbol{G}}_\omega+\boldsymbol{u}_\omega,\end{aligned}\tag{9}$$

where n_{kj}, n_{kgi}, n_{uij} $(k=u,v,w,p,q,r;i=1,2;j=1,2,\ldots,10)$ are known constant coefficients.

4. Path following controller design and analyses

Assuming that all states of the airship are measurable or estimated, the objective of path following control is to calculate the deflections of control surfaces such that the position of the airship tends to a desired planar path $\boldsymbol{\zeta}_c(\varpi)=[x_c(\varpi),y_c(\varpi)]^T$ or a spatial path $\boldsymbol{\zeta}_c(\varpi)=[x_c(\varpi),y_c(\varpi),z_c(\varpi)]^T$, which is differentiable with respect to its parameter ϖ and the other states of the airship are kept bounded. Planar path following control for vehicles remains the mainstream research direction, even for space vehicles such as autonomous underwater vehicles (Bi, Wei, Zhang, & Cao, 2010) and airships (Xie et al., 2007; Zhang et al., 2008), and it is rare to see the study of spatial path following control with experimental results. Therefore, though the planar case is a special version of the spatial case, we first introduce the planar case and extend the discussion to the spatial case to illustrate the adaptability and comprehensiveness of our work for planar vehicles. In addition, a constant propeller speed is maintained in this study rather than a constant flight speed, which is more realistic for the most airship manoeuvring operating conditions.

The path following controller (Fig. 4) for the airship consists of three parts: a guidance loop, an attitude kinematics control loop and an attitude dynamics control loop. The guidance loop, including planar or spatial guidance laws for different missions, calculates the desired attitude $\boldsymbol{\gamma}_c=[\phi_c,\theta_c,\psi_c]^T$, and the attitude control loops are performed based on the TLC theory. Desired attitude is the command followed by the attitude kinematics loop. The corresponding kinematics controller generates the desired angular velocity $\boldsymbol{\omega}_c=[p_c,q_c,r_c]^T$, which is the command for the attitude dynamics loop that follows. A detailed design procedure of each part is described in the following subsections.

4.1. Guidance loop

In this subsection, the required attitude $\boldsymbol{\gamma}_c$ is calculated based on the GBFP principle.

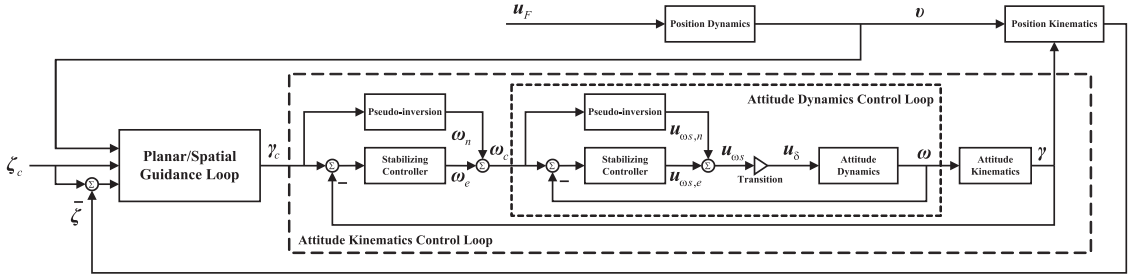

Fig. 4. Structure of the path following controller for airship.

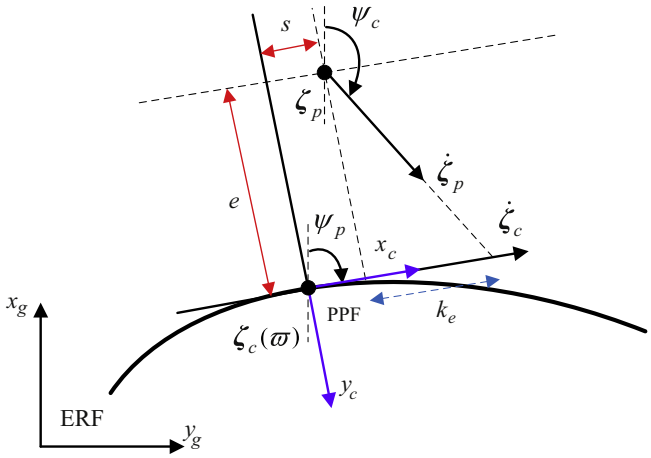

Fig. 5. Geometrical relationship in planar guidance.

4.1.1. Planar guidance law

Suppose that the following attitude control loops have controlled pitch to its command zero. Ignoring the influence of roll, the planar position kinematics equation of (5) is described as follows:

$$\dot{\zeta}_p = \begin{bmatrix} \dot{x} \\ \dot{y} \end{bmatrix} = \begin{bmatrix} \cos\psi & -\sin\psi \\ \sin\psi & \cos\psi \end{bmatrix} \begin{bmatrix} u \\ v \end{bmatrix} \triangleq \boldsymbol{R}(\psi) \begin{bmatrix} u \\ v \end{bmatrix}. \tag{10}$$

Consider the desired continuous path $\zeta_c(\varpi) = [x_c(\varpi), y_c(\varpi)]^T$ to be parameterised by a scalar variable ϖ. Denote a local reference frame, i.e., a path parallel frame (PPF), at $\zeta_c(\varpi)$ (Fig. 5): its x_c-axis is aligned with the tangential vector of the path at $\zeta_c(\varpi)$, and the y_c-axis is perpendicular to x_c-axis and points towards the right. To arrive at the PPF, the ERF should be positively rotated at an angle as follows:

$$\psi_p = \arctan 2(y_c'(\varpi), x_c'(\varpi)), \tag{11}$$

where $(\cdot)_c'(\varpi) \triangleq \mathrm{d}(\cdot)_c/\mathrm{d}\varpi$. Therefore, it has the following expression:

$$\dot{\zeta}_c = \begin{bmatrix} \cos\psi_p & -\sin\psi_p \\ \sin\psi_p & \cos\psi_p \end{bmatrix} \begin{bmatrix} v_p \\ 0 \end{bmatrix} \triangleq \boldsymbol{R}(\psi_p) \begin{bmatrix} v_p \\ 0 \end{bmatrix}, \tag{12}$$

where $\boldsymbol{R}(\psi_p)$ is the rotation matrix from ERF to PPF and $[v_p, 0]^T$ is the velocity of the PPF with respect to the ERF, represented in the PPF. Consequently, the error vector between ζ_p and $\zeta_c(\varpi)$ expressed in the PPF is provided as follows:

$$\boldsymbol{\varepsilon} = [s, e]^T = \boldsymbol{R}^T(\psi_p)(\zeta_p - \zeta_c(\varpi)), \tag{13}$$

where s is the along-track error and e is the cross-track error (Fig. 5). Therefore, the planar path following problem can be solved by driving $\|\boldsymbol{\varepsilon}\| \to 0$.

Suppose that $\psi = \psi_c$ can realise path following for the desired path $\zeta_c(\varpi)$, and denote a positive definite unbounded Lyapunov function as follows:

$$\boldsymbol{V}_\varepsilon = \tfrac{1}{2}\boldsymbol{\varepsilon}^T\boldsymbol{\varepsilon}. \tag{14}$$

By differentiating (14) with respect to time along the trajectory of $\boldsymbol{\varepsilon}$ and using (10) and (12), the equation can be obtained as follows:

$$\begin{aligned} \dot{\boldsymbol{V}}_\varepsilon &= \boldsymbol{\varepsilon}^T\dot{\boldsymbol{\varepsilon}} = \boldsymbol{\varepsilon}^T(\dot{\boldsymbol{R}}^T(\psi_p)(\zeta_p - \zeta_c) + \boldsymbol{R}^T(\psi_p)(\dot{\zeta}_p - \dot{\zeta}_c)) = \boldsymbol{\varepsilon}^T((\boldsymbol{R}(\psi_p)\boldsymbol{S}_p)^T(\zeta_p - \zeta_c) + \boldsymbol{R}^T(\psi_p)(\dot{\zeta}_p - \dot{\zeta}_c)) \\ &= \boldsymbol{\varepsilon}^T\boldsymbol{S}_p^T\boldsymbol{\varepsilon} + \boldsymbol{\varepsilon}^T\boldsymbol{R}^T(\psi_p)(\dot{\zeta}_p - \dot{\zeta}_c) = \boldsymbol{\varepsilon}^T\boldsymbol{R}^T(\psi_p)(\dot{\zeta}_p - \dot{\zeta}_c) \\ &= s(u\cos(\psi_c - \psi_p) - v\sin(\psi_c - \psi_p) - v_p) + e(u\sin(\psi_c - \psi_p) \quad + v\cos(\psi_c - \psi_p)) \\ &= s(u\cos(\psi_c - \psi_p) - v\sin(\psi_c - \psi_p) - \dot{\varpi}\sqrt{x_c'^2 + y_c'^2}) + e(u\sin(\psi_c - \psi_p) + v\cos(\psi_c - \psi_p)), \end{aligned} \tag{15}$$

where

$$\boldsymbol{S}_p = \begin{bmatrix} 0 & -\dot{\psi}_p \\ \dot{\psi}_p & 0 \end{bmatrix}.$$

Choose

$$\psi_c = \psi_p + \arctan 2(-e, k_e) - \arctan 2(v,u) \triangleq \psi_p + \psi_r - \beta_s, \tag{16}$$

$$\dot{\varpi} = \frac{u\cos(\psi_c-\psi_p) - v\sin(\psi_c-\psi_p) + k_s s}{\sqrt{x_c'^2 + y_c'^2}}, \tag{17}$$

where $\{k_s, k_e\} > 0$ are controller parameters given by designers. The derivative of the Lyapunov function (15) can be written as follows:

$$\dot{\boldsymbol{V}}_\varepsilon = -k_s s^2 - \frac{u\sqrt{u^2+v^2}}{|u|\sqrt{e^2+k_e^2}} e^2 = -k_s s^2 - \frac{\sqrt{u^2+v^2}}{\sqrt{e^2+k_e^2}} e^2 \le 0 \quad (\text{if } u > 0). \tag{18}$$

It follows that the path following error $\boldsymbol{\varepsilon}$ is uniformly globally asymptotically stable based on standard Lyapunov arguments on the condition that $u > 0$. Therefore, the desired attitude for planar path following is deduced as $\boldsymbol{\gamma}_c = [0,0,\psi_c]^T$.

4.1.2. Spatial guidance law

The above planar guidance law can be extended to the spatial guidance scenarios. First, the path reference frame (PRF) attached to the airship is defined as follows: its origin O is coincident with CV; the Ox_k-axis points in the direction of speed; the Oz_k-axis is perpendicular to the Ox_k-axis and points downwards; and the Oy_k-axis is determined using the right-hand rule and points towards the right. Then, the associated azimuth and elevation angles can be obtained as follows:

$$\chi = \arctan 2(\dot{y}, \dot{x}), \quad \varphi = \arctan 2\left(-\dot{z}, \sqrt{\dot{x}^2+\dot{y}^2}\right).$$

Consider the desired continuous path $\boldsymbol{\zeta}_c(\varpi) = [x_c(\varpi), y_c(\varpi), z_c(\varpi)]^T$ to be parameterised by a scalar variable ϖ. Referring to the planar guidance law, denote a local reference frame, the PPF, at $\boldsymbol{\zeta}_c(\varpi)$ (Fig. 6) as follows: its x_c-axis is aligned with the tangential vector of the path at $\boldsymbol{\zeta}_c(\varpi)$; the y_c-axis is perpendicular to the x_c-axis and points towards the right; and the z_c-axis is determined by the right-hand rule and points downwards. Therefore, it has the expression of the desired path as follows:

$$\dot{\boldsymbol{\zeta}}_c(\varpi) = \boldsymbol{R}_p [V_p, 0, 0]^T, \tag{19}$$

where V_p is the speed of the reference point $\boldsymbol{\zeta}_c(\varpi)$ in the PPF and

$$\boldsymbol{R}_p = \boldsymbol{R}_{p,z}(\chi_p)\boldsymbol{R}_{p,y}(\varphi_p) = \begin{bmatrix} \cos\chi_p & -\sin\chi_p & 0 \\ \sin\chi_p & \cos\chi_p & 0 \\ 0 & 0 & 1 \end{bmatrix} \begin{bmatrix} \cos\varphi_p & 0 & \sin\varphi_p \\ 0 & 1 & 0 \\ -\sin\varphi_p & 0 & \cos\varphi_p \end{bmatrix} \tag{20}$$

is the full rotation from the PPF to the ERF, with the rotation angles given as follows:

$$\begin{aligned} \chi_p &= \arctan 2(y_c'(\varpi), x_c'(\varpi)), \\ \varphi_p &= \arctan 2\left(-z_c'(\varpi), \sqrt{x_c'(\varpi)^2 + y_c'(\varpi)^2}\right), \end{aligned} \tag{21}$$

which occurs about the $O_g z_g$- and $O_g y_g$-axes. Similarly, the expression for the motion of airship can be given as

$$\dot{\boldsymbol{\zeta}} = \boldsymbol{R}_d [V, 0, 0]^T, \tag{22}$$

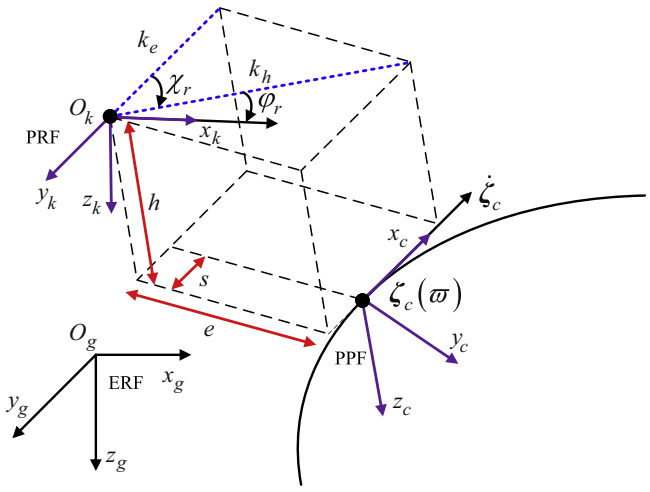

Fig. 6. Geometrical relationship in spatial guidance.

where $\boldsymbol{R}_d$ is the rotation matrix from the PRF to the ERF, which is denoted as follows:

$$\boldsymbol{R}_d = \boldsymbol{R}_{d,z}(\chi_d)\boldsymbol{R}_{d,y}(\varphi_d) \triangleq \boldsymbol{R}_p\boldsymbol{R}_r = \boldsymbol{R}_p\boldsymbol{R}_{r,z}(\chi_r)\boldsymbol{R}_{r,y}(\varphi_r), \tag{23}$$

with the rotation angles $\{\chi_d,\varphi_d\}$ are similar to (20) from the PRF to the ERF and $\{\chi_r,\varphi_r\}$ from the PRF to the PPF. Consequently, the error vector between ζ and $\zeta_c(\varpi)$ expressed in the PPF is provided as follows:

$$\boldsymbol{\varepsilon} = [s,\ e,\ h]^{\mathrm{T}} = \boldsymbol{R}_p^{\mathrm{T}}(\boldsymbol{\zeta}-\boldsymbol{\zeta}_c(\varpi)), \tag{24}$$

where s is the along-track error, e is the cross-track error and h is the vertical-track error (Fig. 6). Therefore, the spatial path following problem can be solved by driving $\|\boldsymbol{\varepsilon}\| \to 0$.

The positive definite unbounded Lyapunov function can be denoted as follows:

$$\boldsymbol{V}_\varepsilon = \tfrac{1}{2}\boldsymbol{\varepsilon}^{\mathrm{T}}\boldsymbol{\varepsilon}. \tag{25}$$

Differentiating (25) with respect to time along the trajectory of $\boldsymbol{\varepsilon}$ and using (19), (22) and (23), the equation can be obtained as follows:

$$\begin{aligned}\dot{\boldsymbol{V}}_\varepsilon &= \boldsymbol{\varepsilon}^{\mathrm{T}}\dot{\boldsymbol{\varepsilon}} = \boldsymbol{\varepsilon}^{\mathrm{T}}(\dot{\boldsymbol{R}}_p^{\mathrm{T}}(\zeta-\zeta_c)+\boldsymbol{R}_p^{\mathrm{T}}(\dot{\zeta}-\dot{\zeta}_c)) = \boldsymbol{\varepsilon}^{\mathrm{T}}\boldsymbol{S}_p^{\mathrm{T}}\boldsymbol{\varepsilon}+\boldsymbol{\varepsilon}^{\mathrm{T}}\boldsymbol{R}_p^{\mathrm{T}}(\dot{\zeta}-\dot{\zeta}_c) = \boldsymbol{\varepsilon}^{\mathrm{T}}\boldsymbol{R}_p^{\mathrm{T}}(\dot{\zeta}-\dot{\zeta}_c)\\ &= s(V\cos\chi_r\cos\varphi_r - V_p)+eV\sin\chi_r\cos\varphi_r - hV\sin\varphi_r\\ &= s(V\cos\chi_r\cos\varphi_r - \dot{\varpi}\sqrt{x_c'^2+y_c'^2+z_c'^2})+eV\sin\chi_r\cos\varphi_r - hV\sin\varphi_r,\end{aligned} \tag{26}$$

where

$$\boldsymbol{S}_p = \begin{bmatrix} 0 & -\dot{\chi}_p\cos\varphi_p & \dot{\varphi}_p \\ \dot{\chi}_p\cos\varphi_p & 0 & \dot{\chi}_p\sin\varphi_p \\ -\dot{\varphi}_p & -\dot{\chi}_p\sin\varphi_p & 0 \end{bmatrix}.$$

Choose

$$\chi_r = \arctan 2(-e,k_e), \quad \varphi_r = \arctan 2(h,k_h), \tag{27}$$

$$\dot{\varpi} = \frac{V\cos\chi_r\cos\varphi_r + k_s s}{\sqrt{x_c'^2+y_c'^2+z_c'^2}}, \tag{28}$$

where $\{k_e,k_s,k_h\} > 0$ are controller parameters given by designers, the derivative of Lyapunov function (25) finally becomes

$$\dot{\boldsymbol{V}}_\varepsilon = -k_s s^2 - \frac{V\cos\varphi_r}{\sqrt{e^2+k_e^2}}e^2 - \frac{V}{\sqrt{h^2+k_h^2}}h^2 \le 0 \quad (\text{if } V>0). \tag{29}$$

It follows that the path following error $\boldsymbol{\varepsilon}$ is globally uniformly asymptotically stable based on standard Lyapunov arguments under the condition $V > 0$. Consequently, we obtain $\{\chi_d,\varphi_d\}$ from (23) as follows:

$$\chi_d = \arctan\left(\frac{\cos\chi_p\sin\chi_r\cos\varphi_r - \sin\varphi_p\sin\varphi_r\sin\chi_p + \sin\chi_p\cos\chi_r\cos\varphi_p\cos\varphi_r}{-\sin\chi_p\sin\chi_r\cos\varphi_r - \sin\varphi_p\sin\varphi_r\cos\chi_p + \cos\chi_p\cos\chi_r\cos\varphi_p\cos\varphi_r}\right), \tag{30}$$

$$\varphi_d = \arcsin(\sin\varphi_p\cos\varphi_r\cos\chi_r + \cos\varphi_p\sin\varphi_r). \tag{31}$$

The desired attitude is deduced as $\boldsymbol{\gamma}_c = [0,\varphi_d-\alpha,\chi_d-\beta]^T$ (Breivik & Fossen, 2005a), where α is the angle-of-attack and β is the sideslip angle.

4.2. Attitude control loops

In this subsection, the required deflection of the rudders $\boldsymbol{u}_\delta$ to achieve the command attitude $\boldsymbol{\gamma}_c$ is calculated.

4.2.1. Attitude kinematics control loop

The pseudo-inversion of attitude kinematics is derived from (6) as follows:

$$\boldsymbol{\omega}_n = \boldsymbol{R}_\gamma^{-1}(\boldsymbol{\gamma}_c)\dot{\boldsymbol{\gamma}}_c, \tag{32}$$

where $\dot{\boldsymbol{\gamma}}_c$ is obtained from the pseudo-differentiator (4) and $\boldsymbol{\gamma}_c$. By defining the error vector $\boldsymbol{\gamma}_{err} \triangleq \boldsymbol{\gamma}-\boldsymbol{\gamma}_c$, the linearisation of the error equation can be obtained as follows:

$$\dot{\boldsymbol{\gamma}}_{err} = \boldsymbol{R}_\gamma(\boldsymbol{\gamma}_c)\boldsymbol{\omega}_e.$$

Furthermore, defining augmented error vector (Zhu & Huo, 2010) $\boldsymbol{\gamma}_a = [\int \boldsymbol{\gamma}_{err}^T\,dt, \boldsymbol{\gamma}_{err}^T]^T$ gives the augmented error equation

$$\dot{\boldsymbol{\gamma}}_a = \overline{\boldsymbol{A}}_\gamma\boldsymbol{\gamma}_a + \overline{\boldsymbol{B}}_\gamma\boldsymbol{\omega}_e,$$

where

$$\overline{\boldsymbol{A}}_\gamma = \begin{bmatrix} \boldsymbol{O}_3 & \boldsymbol{I}_3 \\ \boldsymbol{O}_3 & \boldsymbol{O}_3 \end{bmatrix}, \quad \overline{\boldsymbol{B}}_\gamma = \begin{bmatrix} \boldsymbol{O}_3 \\ \boldsymbol{R}_\gamma \end{bmatrix},$$

$\boldsymbol{O}_3$ and $\boldsymbol{I}_3$ are three-dimensional zero matrix and identity matrix, respectively.

Design a time-varying control law

$$\boldsymbol{\omega}_e = -\boldsymbol{K}_{\gamma,I}\int \boldsymbol{\gamma}_{err}\,dt - \boldsymbol{K}_{\gamma,P}\boldsymbol{\gamma}_{err} \triangleq -\boldsymbol{K}_{\gamma}(t)\boldsymbol{\gamma}_a \tag{33}$$

such that

$$\dot{\boldsymbol{\gamma}}_a = [\overline{\boldsymbol{A}}_{\gamma} - \overline{\boldsymbol{B}}_{\gamma}\boldsymbol{K}_{\gamma}]\boldsymbol{\gamma}_a = \overline{\boldsymbol{A}}_1\boldsymbol{\gamma}_a, \tag{34}$$

where

$$\overline{\boldsymbol{A}}_1 = \begin{bmatrix} \boldsymbol{O}_3 & \boldsymbol{I}_3 \\ \begin{matrix} a_{111} & & \\ & a_{112} & \\ & & a_{113} \end{matrix} & \begin{matrix} a_{121} & & \\ & a_{122} & \\ & & a_{123} \end{matrix} \end{bmatrix} = \begin{bmatrix} \boldsymbol{O}_3 & \boldsymbol{I}_3 \\ \hat{\boldsymbol{A}}_{\gamma,1} & \hat{\boldsymbol{A}}_{\gamma,2} \end{bmatrix},$$

$$a_{11k} = -\omega_{1k}^2, \quad a_{12k} = -2\xi_{1k}\omega_{1k}, \quad k = 1,2,3. \tag{35}$$

It is obvious that the closed-loop system (34) is a linear time-invariant system whose poles can be assigned arbitrarily, and it is decoupled to three subsystems. The dynamic behaviour of each subsystem can be designed arbitrarily by choosing ξ_{1k} and ω_{1k}: for a given ξ_{1k}, a larger ω_{1k} leads to a faster convergence of subsystem states. Using (34), the time-varying feedback matrix $\boldsymbol{K}_{\gamma}(t)$ can be obtained as follows:

$$\boldsymbol{K}_{\gamma,I} = -\boldsymbol{R}_{\gamma}^{-1}(\boldsymbol{\gamma}_c)\hat{\boldsymbol{A}}_{\gamma,1}, \quad \boldsymbol{K}_{\gamma,P} = -\boldsymbol{R}_{\gamma}^{-1}(\boldsymbol{\gamma}_c)\hat{\boldsymbol{A}}_{\gamma,2}.$$

Based on the TLC theory, the desired angular velocity $\boldsymbol{\omega}_c = \boldsymbol{\omega}_n + \boldsymbol{\omega}_e$ is the reference command for the attitude dynamics control loop.

4.2.2. Attitude dynamics control loop

The pseudo-inversion of attitude dynamics can be derived as follows:

$$\boldsymbol{u}_{\omega s,n} = \begin{bmatrix} q_n \\ r_n \end{bmatrix} = \dot{\boldsymbol{\omega}}_{s,c} - \begin{bmatrix} \overline{\boldsymbol{N}}_{\omega}(2)|_{\boldsymbol{\omega}_{s,c}} \\ \overline{\boldsymbol{N}}_{\omega}(3)|_{\boldsymbol{\omega}_{s,c}} \end{bmatrix} - \begin{bmatrix} \overline{\boldsymbol{G}}_{\omega}(2)|_{\boldsymbol{\omega}_{s,c}} \\ \overline{\boldsymbol{G}}_{\omega}(3)|_{\boldsymbol{\omega}_{s,c}} \end{bmatrix}, \tag{36}$$

where $\{\overline{\boldsymbol{N}}_{\omega}(i), \overline{\boldsymbol{G}}_{\omega}(i)\}$, $(i = 2,3)$ represent the ith row of $\{\overline{\boldsymbol{N}}_{\omega}, \overline{\boldsymbol{G}}_{\omega}\}$ and $\dot{\boldsymbol{\omega}}_{s,c} \triangleq [\dot{q}_c, \dot{r}_c]^T$ is obtained from the pseudo-differentiator (4). The linearisation of the error equation can be obtained as

$$\dot{\boldsymbol{\omega}}_{s,e} = \tilde{\boldsymbol{A}}_{\omega}\boldsymbol{\omega}_{s,e} + \tilde{\boldsymbol{B}}_{\omega}\boldsymbol{u}_{\omega s,e},$$

where $\boldsymbol{\omega}_{s,e} \triangleq \boldsymbol{\omega}_s - \boldsymbol{\omega}_{s,c}$, $\boldsymbol{\omega}_s \triangleq [q,r]^T$,

$$\tilde{\boldsymbol{A}}_{\omega} = \begin{bmatrix} n_{q3}u_c + 2n_{q5}q_c & 2n_{q6}r_c \\ n_{r3}r_c & n_{r1}u_c \end{bmatrix}, \quad \tilde{\boldsymbol{B}}_{\omega} = \boldsymbol{I}_2.$$

Defining augmented error vector $\boldsymbol{\omega}_{s,a} = [\int \boldsymbol{\omega}_{s,e}^T\,dt, \boldsymbol{\omega}_{s,e}^T]^T$ gives the augmented error equation

$$\dot{\boldsymbol{\omega}}_{s,a} = \overline{\boldsymbol{A}}_{\omega}\boldsymbol{\omega}_{s,a} + \overline{\boldsymbol{B}}_{\omega}\boldsymbol{u}_{\omega s,e},$$

where

$$\overline{\boldsymbol{A}}_{\omega} = \begin{bmatrix} \boldsymbol{O}_2 & \boldsymbol{I}_2 \\ \boldsymbol{O}_2 & \tilde{\boldsymbol{A}}_{\omega} \end{bmatrix}, \quad \overline{\boldsymbol{B}}_{\omega} = \begin{bmatrix} \boldsymbol{O}_2 \\ \tilde{\boldsymbol{B}}_{\omega} \end{bmatrix}.$$

Referring to the design method for the attitude kinematics control loop, a time-varying feedback controller can be designed thus

$$\boldsymbol{u}_{\omega s,e} = -\boldsymbol{K}_{\omega}(t)\boldsymbol{\omega}_{s,a}, \quad \boldsymbol{K}_{\omega}(t) = [-\tilde{\boldsymbol{B}}_{\omega}^{-1}\hat{\boldsymbol{A}}_{\omega,1}, \tilde{\boldsymbol{B}}_{\omega}^{-1}(\tilde{\boldsymbol{A}}_{\omega} - \hat{\boldsymbol{A}}_{\omega,2})], \tag{37}$$

where $\hat{\boldsymbol{A}}_{\omega,1}$ and $\hat{\boldsymbol{A}}_{\omega,2}$ are assigned the same way as $\hat{\boldsymbol{A}}_{\gamma,1}$ and $\hat{\boldsymbol{A}}_{\gamma,2}$ in (35): their diagonal elements are $a_{21k} = -\omega_{2k}^2$ and $a_{22k} = -2\xi_{2k}\omega_{2k}$ $(k = 1,2)$; additionally, ξ_{2k} and ω_{2k} should be chosen properly to guarantee the stability and good dynamic behaviour of the closed-loop subsystems.

Following the TLC theory, $\boldsymbol{u}_{\omega s} = [\boldsymbol{u}_{\omega}(2), \boldsymbol{u}_{\omega}(3)]^T = \boldsymbol{u}_{\omega s,n} + \boldsymbol{u}_{\omega s,e}$. Then, the control of the surfaces can be calculated thus

$$\boldsymbol{u}_{\delta} = \begin{bmatrix} 0 & \dfrac{1}{n_{u15}\mathrm{Q}} \\ \dfrac{1}{n_{u14}\mathrm{Q}} & 0 \end{bmatrix} \left(\boldsymbol{u}_{\omega s} - \begin{bmatrix} n_{u12} & n_{u13} \\ 0 & 0 \end{bmatrix} \boldsymbol{u}_F \right). \tag{38}$$

4.3. Control algorithm

According to the previous design process, the algorithm of the above path following controller for the autonomous airship can be conveniently implemented in the following sequence of steps:

Step 1: Let the control of propulsive force and rotation angle of propellers be constant: $F_T = C_1, \mu = C_2, \{C_1, C_2\} \in \mathbb{R}$; obtain the control vector provided by propellers $\boldsymbol{u}_F = [2F_T \cos\mu, 2F_T \sin\mu]^T$.

Step 2 (planar): Obtain the desired yaw ψ_c from (16); update ϖ from (17); acquire the desired attitude $\boldsymbol{\gamma}_c = [0,0,\psi_c]^T$.

Step 2 (spatial): Obtain the desired azimuth χ_d and elevation φ_d from (30) and (31); update ϖ from (28); acquire the desired attitude $\boldsymbol{\gamma}_c = [0, \varphi_d - \alpha, \chi_d - \beta]^T$.

Step 3: Calculate $\boldsymbol{\omega}_n = \boldsymbol{R}_\gamma^{-1}(\boldsymbol{\gamma}_c)\dot{\boldsymbol{\gamma}}_c$; assign $\hat{\boldsymbol{A}}_{\gamma,1}$ and $\hat{\boldsymbol{A}}_{\gamma,2}$ using (35); calculate $\boldsymbol{K}_{\gamma,I} = -\boldsymbol{R}_\gamma^{-1}(\boldsymbol{\gamma}_c)\hat{\boldsymbol{A}}_{\gamma,1}$, $\boldsymbol{K}_{\gamma,P} = -\boldsymbol{R}_\gamma^{-1}(\boldsymbol{\gamma}_c)\hat{\boldsymbol{A}}_{\gamma,2}$ and $\boldsymbol{\omega}_e = -\boldsymbol{K}_{\gamma,I}\int \boldsymbol{\gamma}_{err}\,dt - \boldsymbol{K}_{\gamma,P}\boldsymbol{\gamma}_{err}$; obtain the desired angular velocity $\boldsymbol{\omega}_c = \boldsymbol{\omega}_n + \boldsymbol{\omega}_e$.

Step 4: Calculate $\boldsymbol{u}_{\omega s,n}$ using (36); assign $\hat{\boldsymbol{A}}_{\omega,1}$ and $\hat{\boldsymbol{A}}_{\omega,2}$ in the same way as (35); calculate $\boldsymbol{u}_{\omega s,e}$ from (37); obtain $\boldsymbol{u}_{\omega s} = \boldsymbol{u}_{\omega s,n} + \boldsymbol{u}_{\omega s,e}$; acquire the actual control of surfaces by (38).

4.4. Stability analysis

Before analysing the stability of the entire closed-loop system under the proposed path following control algorithm, the time scales separation principle (Hovakimyan, Lavretsky, & Cao, 2008; Schumacher & Khargonekar, 1998), which is widely used for aerospace systems (Naidu & Calise, 2001), should be introduced.

Consider a system composed of two subsystems which are shown as follows:

$$\dot{\boldsymbol{x}}_s = \boldsymbol{f}(\boldsymbol{x}_s, \boldsymbol{z}_s), \tag{39}$$

$$\dot{\boldsymbol{z}}_s = \boldsymbol{g}(\boldsymbol{x}_s, \boldsymbol{z}_s), \tag{40}$$

where the origin $\{\boldsymbol{x}_s, \boldsymbol{z}_s\} = \{0,0\}$ is an equilibrium point of the system. Assume that the convergence rate of the subsystem (40) is faster than that of the subsystem (39). Let $\boldsymbol{z}_s = \boldsymbol{h}(\boldsymbol{x}_s)$ be a root of $\boldsymbol{g}(\boldsymbol{x}_s, \boldsymbol{z}_s) = 0$; the reduced system of the subsystem (39) can be expressed as follows:

$$\dot{\boldsymbol{x}}_s = \boldsymbol{f}(\boldsymbol{x}_s, \boldsymbol{h}(\boldsymbol{x}_s)). \tag{41}$$

Because subsystem (40) converges faster, $\boldsymbol{x}_s$ can be treated as a fixed parameter in (41). Define $\boldsymbol{y}_s = \boldsymbol{z}_s - \boldsymbol{h}(\boldsymbol{x}_s)$ to shift the equilibrium point of subsystem (40) to the origin and the reduced system of subsystem (40) can be obtained as follows (Khalil, 2002):

$$\dot{\boldsymbol{y}}_s = \boldsymbol{g}(\boldsymbol{x}_s, \boldsymbol{y}_s + \boldsymbol{h}(\boldsymbol{x}_s)). \tag{42}$$

The time scales separation principle is presented as the following simplified proposition.

Proposition 1. *Assuming that the origins of the reduced systems both (41) and (42) are asymptotically stable, the origin of system (39) and (40) will be asymptotically stable, provided that the fast subsystem (40) converges fast enough.*

A rigorous theoretical proof of the above time scales separation principle has been previously presented (Khalil, 2002, Chapter 11). Based on Proposition 1, the stability of the closed-loop system under the proposed path following control algorithm can be proven in the following proposition.

Proposition 2. *Assuming that the controller parameters satisfy* $\omega_{2j} \gg \omega_{1k} \gg \{k_s, 1/k_e, 1/k_h\}$, $(k = 1,2,3; j = 1,2)$, *the system controlled by the path following control method proposed in this report is asymptotically stable.*

Proof. The stability of the attitude control loop is analysed first. The attitude dynamics control loop has a basic TLC structure. According to the TLC theory, this loop is asymptotically stable (Liu & Zhu, 2007a), which indicates that the attitude dynamics control loop can approximately be considered as an identity matrix; the attitude kinematics control loop is equivalently demonstrated in Fig. 7. The loop is still a basic structure of TLC and is asymptotically stable. From Proposition 1, the stability of the entire attitude control loop is warranted, while the inner dynamics loop is designed to be faster than the outer kinematics loop (i.e., $\omega_{2j} \gg \omega_{1k}$). A rigorous stability proof of this TLC cascaded structure has previously been presented (Liu & Zhu, 2007b). Furthermore, because the reduced system of guidance loop is asymptotically stable, based on Proposition 1, the guidance loop will be asymptotically stable if the attitude control loops converges fast enough (i.e., $\omega_{1k} \gg \{k_s, 1/k_e, 1/k_h\}$).

In conclusion, while designing the attitude dynamics control loop as the fast loop ($\omega_{2j} \gg \omega_{1k}$), the attitude kinematics control loop as the slow loop ($\omega_{1k} \gg \{k_s, 1/k_e, 1/k_h\}$), and the guidance loop as the super-slow loop, the entire closed-loop system controlled by the path following control method will be asymptotically stable. □

4.5. Path following direction analysis

Because the desired path $\boldsymbol{\zeta}_c(\varpi)$ has no definite directional character, it is essential to analyse the path following direction under the proposed method, which is concluded as the following proposition.

Proposition 3. *The path following controller drives the autonomous airship to follow the desired path* $\boldsymbol{\zeta}_c(\varpi)$ *along the direction that* ϖ *increases. If* $\varpi \in (-C, C)$, $C \in \mathbb{R}^+$, *the following direction will be inversed by turning* $\boldsymbol{\zeta}_c(\varpi)$ *into* $\boldsymbol{\zeta}_c(-\varpi)$.

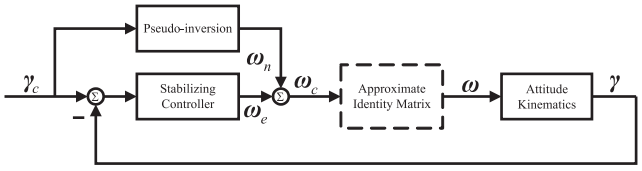

Fig. 7. Equivalent structure of the attitude kinematics control loop.

Proof. Because the error set $\boldsymbol{\varepsilon}$ tends to zero, it deduces that $\{\psi_r,\chi_r,\varphi_r\}\to 0$. Then, following (16) or (28), the following conclusion can be drawn:

$$\dot{\varpi}=\frac{\sqrt{u^2+v^2}}{\sqrt{x_c'^2+y_c'^2}}>0 \quad \text{or} \quad \dot{\varpi}=\frac{V}{\sqrt{x_c'^2+y_c'^2+z_c'^2}}>0,$$

while implementing the planar or spatial path following mission, which means that the control method drives the autonomous airship following the path in the direction along with ϖ increases. In addition, if $\varpi\in(-C,C)$, $C\in\mathbb{R}^+$, $\zeta_c(-\varpi)$ presents the same path as $\zeta_c(\varpi)$ but in an inverse direction, while $\dot{\varpi}>0$. Therefore, for the proposed path following control method, the following direction is determined for a given desired path $\zeta_c(\varpi)$, and it is convenient to change the following direction by turning $\zeta_c(\varpi)$ to $\zeta_c(-\varpi)$. □

5. Flight experiments

In this section, the flight experiments for the autonomous airship are conducted to verify the proposed path following control method. The airship (Fig. 2) is refitted from a LS-S1200 type airship of the Beijing Lonsan United Aviation Technology Company (Lonsan, 2012). After introducing the experimental parameters, system and process, the experimental results of attitude tracking, planar path following and spatial path following are illustrated in the following subsections.

5.1. Experimental parameters, system and process

The configuration parameters of the autonomous airship are demonstrated in Fig. 8, where the length, maximum diameter and volume of the ballonet are 13.2 m, 3.38 m and 80 m^3, respectively. The total mass of the airship is 100 kg. In addition, the coordinates of the CV $\{x_g,z_g\}=\{0,1.54\}$ m, the ellipsoid inertia factors $\{k_1,k_2,k_3\}=\{0.14,0.86.0.35\}$, and the torques of inertia $\{I_x,I_y,I_z\}=\{324,650,371\}$ kg m^2 are calculated. The controller parameters are shown in Table 1, which satisfies the time scales separation requirement of Proposition 2.

The airship platform, whose flight control system is illustrated in Fig. 9, can perform a continuous flight of less than 2 h for each sortie; the flight time is restrained by the filled oil amount and the power of the diesel engine. The system's integrated navigation device (IND) is developed by Xsens Technologies with a type of MTi-G (Xsens, 2012). The MTi-G is an integrated Global Position System (GPS) and inertial measurement unit with a navigation and attitude and heading reference system processor. It can provide airship states, including position, attitude, velocity and angular velocity. Using these parameters, the flight control computer executes the designed path following control law and calculates the control values to be transmitted to the steering engines of the rudders and elevators. The sampling frequency in the flight experiments is 20 Hz, and the maximum deflections of the rudders and elevators are set to 24° for safety. In addition, a remote controller and a ground station are equipped to determine the telemetry and telecontrol functions by a wireless link whose maximum communication range is 1 km. The ground station can display and save the airship states in real time and can adjust controller parameters and the flight mode on-line. The flight control system and software for airships have previously been studied (Zheng, Zhu, & Jiang, 2009) through which we performed the detailed design and showed the analysis of software performance.

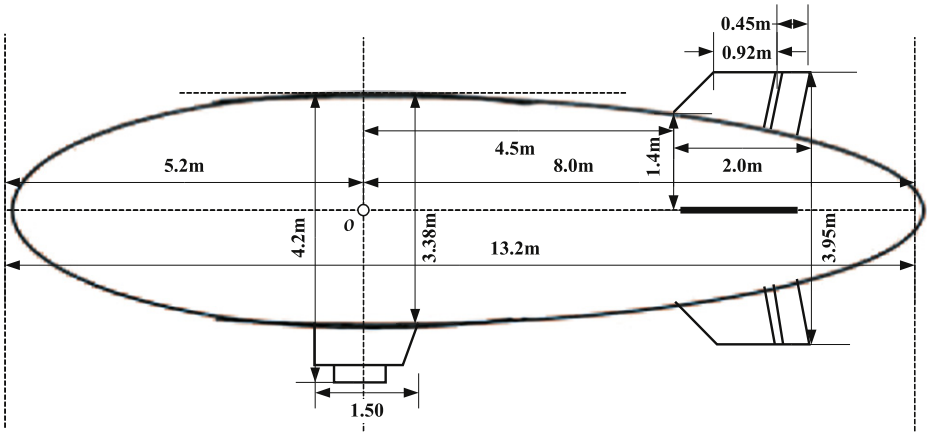

Fig. 8. Configuration parameters of the autonomous airship.

Table 1
Controller parameters in flight experiments.

Guidance loop		Kinematics loop		Dynamics loop	
Notations	Values	Notations (k=1,2,3)	Values	Notations (j=1,2)	Values
k_s	0.01	ω_d	0.5	ω_d	0.5
k_e	100	ξ_{1k}	2	ξ_{2j}	2
k_h	100	ω_{1k}	0.1	ω_{2j}	0.4

In our experiments, the airship was released in Miyun County of Beijing on 14 September 2011, and there was an intermittent light breeze (1.6–3.3 m/s). During the experiments, the airship was manually operated to reach a specific altitude. Then, the airship was switched to the autonomous mode controlled by the proposed path following control algorithm. Because the guidance loop is stable if the airship speed $V>0$, the constant propulsive force ($F_T=C_1>0$) and zero rotation angle ($\mu=0$) of the propellers were specified to keep the cruise speed at approximately 8 m/s. When the experiments were completed, the control administration was returned to the manipulator, and the airship performed a landing under the manual manipulation mode.

5.2. Attitude tracking experiment

To verify the effectiveness of the inner attitude control loops, the attitude tracking experiment was first carried out with the desired pitch set as 10° and the desired yaw set as 80°. As indicated in Figs. 10 and 11, the attitude tracking controller based on the TLC theory can force the airship to track a desired attitude with a control precision of less than 2°.

Remark. The controller parameters were chosen to be overdamped. However, there was still an overshoot in attitude tracking for the following possible reasons: (1) the airship was lightweight with a large volume, which led it to have small damping and great reactive

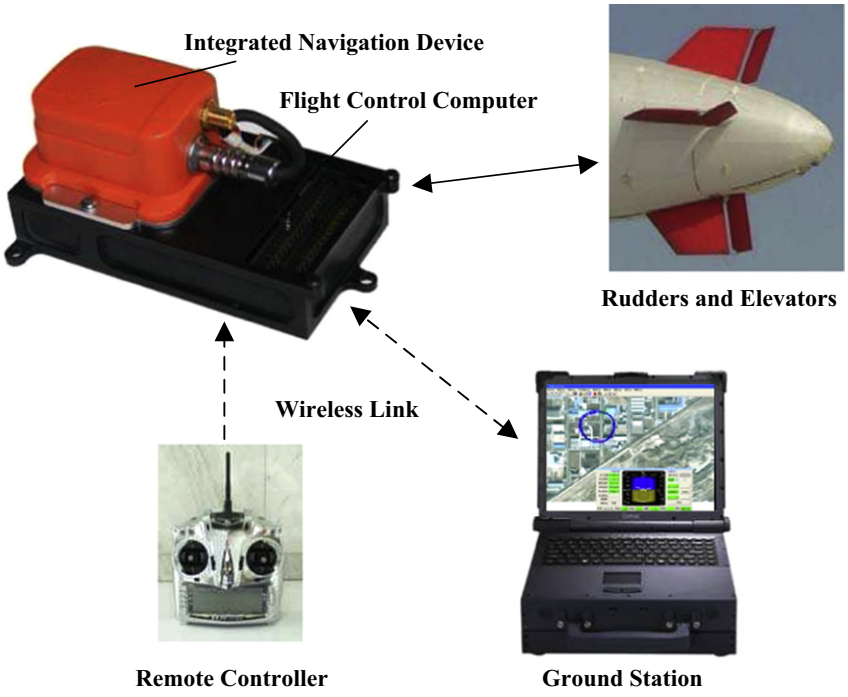

Fig. 9. Flight control system of the autonomous airship.

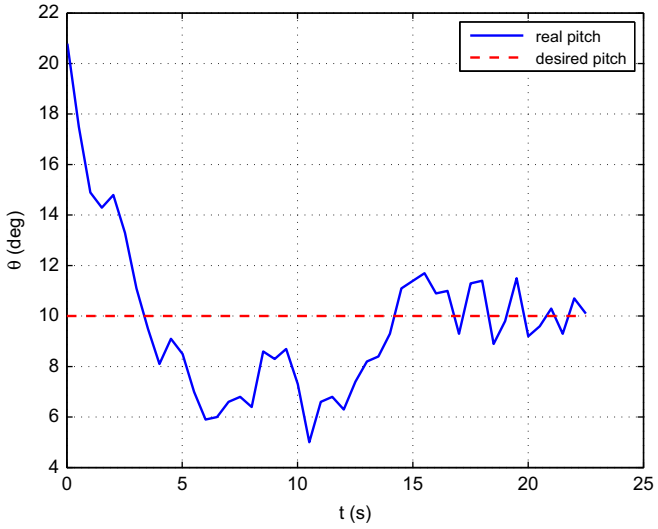

Fig. 10. Experimental result of pitch tracking.

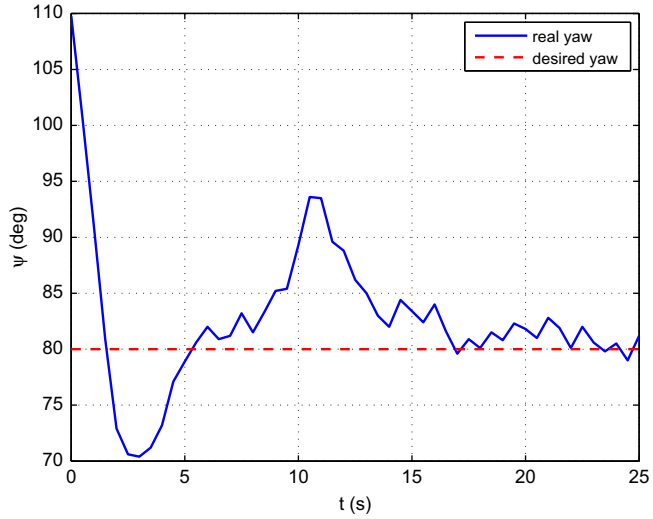

Fig. 11. Experimental result of yaw tracking.

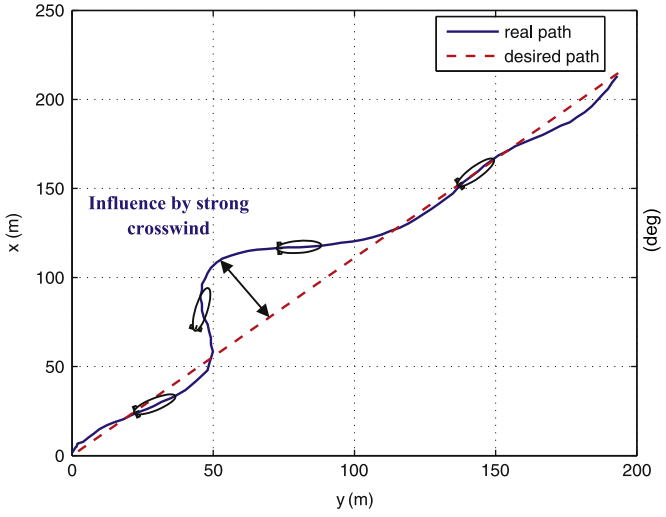

Fig. 12. Position of planar line path following experiment.

sensitivity; (2) the model parameters of the airship for controller calculation were imprecise and contained uncertainty; and (3) there was wind disturbance. Influenced by these three factors, the expected overdamped system became underdamped. This problem can be solved by adjusting the controller parameters.

5.3. *Planar path following experiments*

The planar path following experiments, including straight-line path following and circle path following, were implemented to verify the proposed planar path following control method.

5.3.1. *Line path following*

The desired path for the planar straight-line path following experiment is given as

$$\zeta_c(\varpi) = [x_c(\varpi), y_c(\varpi)]^T = [\varpi \cos \psi_0, \varpi \sin \psi_0]^T,$$

where ψ_0 is the yaw of the airship while switching the flight mode from manual to autonomous. The experimental results of position and attitude are shown in Figs. 12 and 13, respectively. Due to a gust of unexpected strong crosswind, the airship flew off the course by approximately 20 m (Fig. 12) in the beginning of the experiment. However, the airship converged to the desired line again when the strong disturbance vanished, which verified the performance of our control method.

5.3.2. *Circle path following*

The desired path for the planar circle path following experiment is given as

$$\zeta_c(\varpi) = [x_c(\varpi), y_c(\varpi)]^T = [k_r \sin \varpi - k_r \sin \psi_0, -k_r \cos \varpi + k_r \cos \psi_0]^T,$$

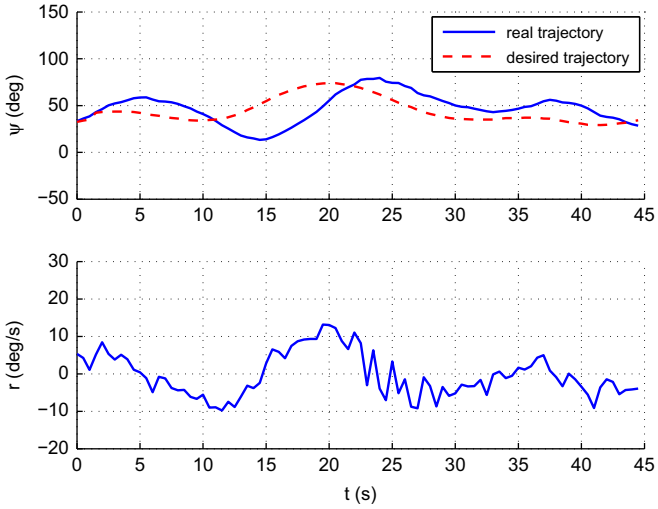

Fig. 13. Attitude of planar line path following experiment.

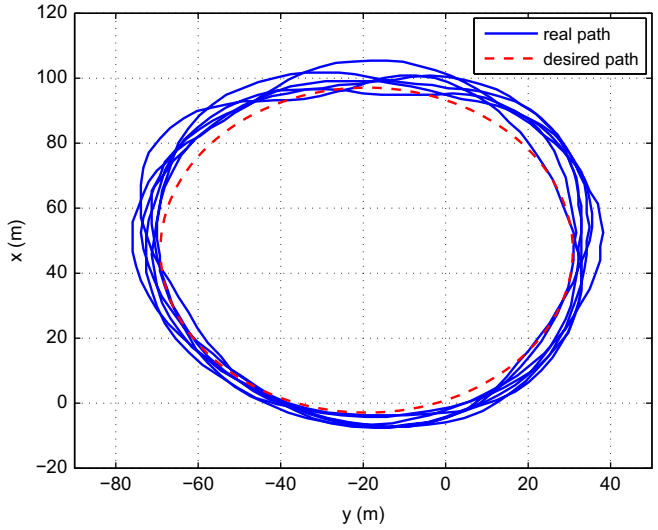

Fig. 14. Position of planar circle path following experiment.

where ψ_0 is the yaw of the airship while switching the flight mode from manual to autonomous, and $k_r = 50$ m is the radius of the desired circle. It is observed from the above definition and Proposition 3 that the airship is expected to implement a clockwise path following with the initial yaw tangent to the desired circle.

The experiment lasted for approximately 7 min and the airship successfully circled the desired path 10 times. Partial experimental results of position and attitude are shown in Figs. 14 and 15, respectively, and the results of tracking error and control variable are shown in Figs. 16 and 17, respectively. As indicated in Figs. 14 and 16, in the presence of the unknown wind disturbance, the cross-track error e is maintained within 10 m most of the time. The position errors of Xie et al. (2007) and Miller et al. (2007) are 55 m and 30 m, respectively, which illustrate the excellent performance of our control method. However, it does not mean that our method is better than the previous methods (Xie et al., 2007; Miller et al., 2007) because these experiments were implemented in different airships and weather conditions. Our experimental results indicate that the planar path following control method is feasible and that the airship can track a mission path with satisfactory precision.

5.4. Spatial path following experiments

The spatial path following experiments, including ascending straight-line path following and helix path following, were implemented to verify the proposed spatial path following control method.

5.4.1. Line path following

The desired path for the ascending straight-line path following experiment is given as

$$\zeta_c(\varpi) = [x_c(\varpi), y_c(\varpi), z_c(\varpi)]^T = [\varpi \cos\psi_0, \varpi \sin\psi_0, -k_a\varpi]^T,$$

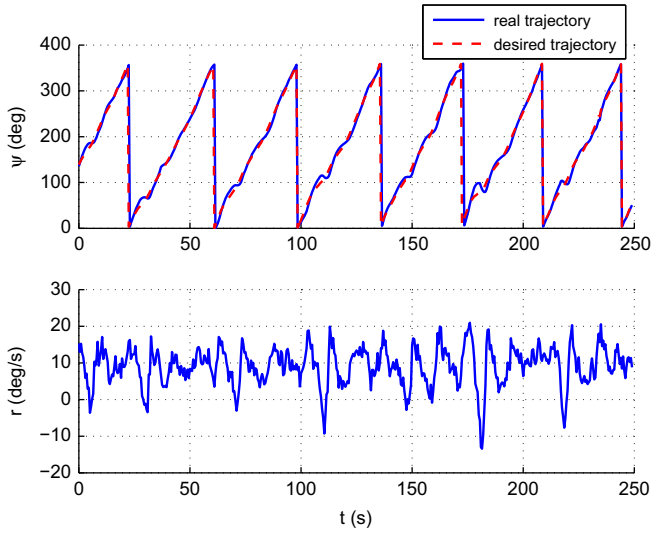

Fig. 15. Attitude of planar circle path following experiment.

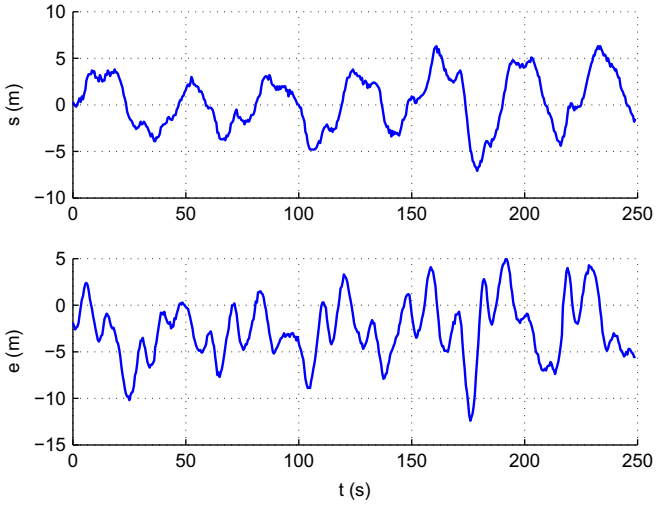

Fig. 16. Tracking error of planar circle path following experiment.

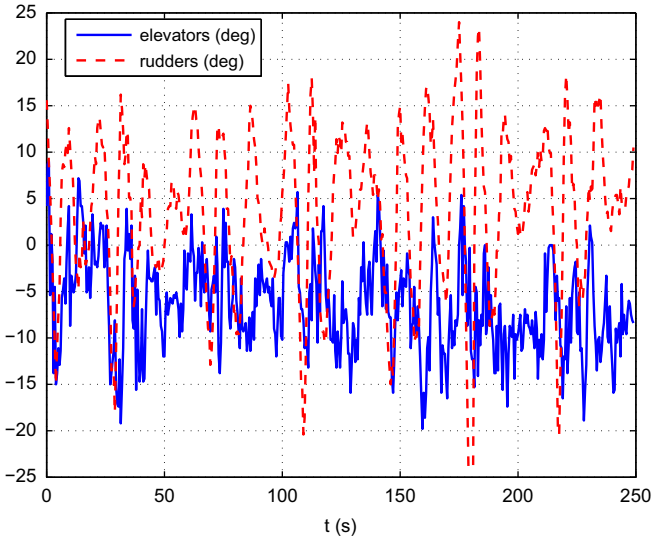

Fig. 17. Control variable of planar circle path following experiment.

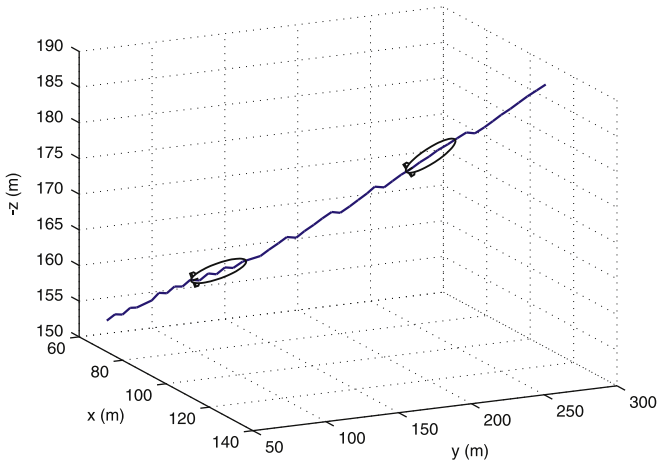

Fig. 18. Position of spatial line path following experiment.

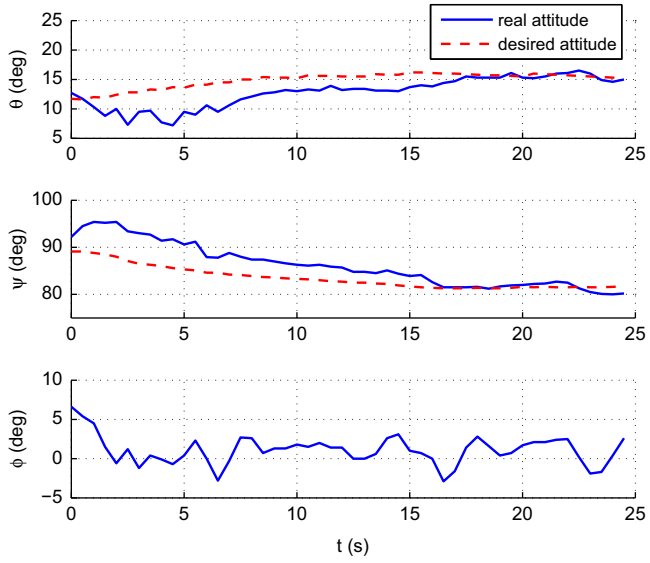

Fig. 19. Attitude of spatial line path following experiment.

where ψ_0 is the yaw of the airship while switching the flight mode from manual to autonomous and k_a denotes the rate of climb. The experimental results of position and attitude are shown in Figs. 18 and 19, respectively, which establish that the spatial path following control method is feasible.

5.4.2. Helix path following

The desired path for the ascending helix path following experiment is given as

$$\zeta_c(\varpi) = [x_c(\varpi), y_c(\varpi), z_c(\varpi)]^T = [k_r \sin \varpi - k_r \sin \psi_0, -k_r \cos \varpi + k_r \cos \psi_0, -k_a \varpi]^T,$$

where ψ_0 is the yaw of the airship while switching the flight mode from manual to autonomous, $k_r = 50$ m is the radius of planar projection circle, and k_a denotes the rate of climb. The experiment lasted for approximately 4 min, constrained by the effective range of the wireless link, and the airship successfully circled the desired path five times. Partial experimental results of spatial position, altitude and planar position are shown in Figs. 20, 21, and 22, and the results of attitude, tracking error and control variable in Figs. 23, 24 and 25.

Due to the lower accuracy of the equipped IND sensor and the unknown wind perturbations, the position data, especially the altitude shown in Fig. 21, are oscillated. As indicated in Figs. 22 and 24, in the presence of unknown wind disturbance, the cross-track error e and the vertical-track error h are maintained within 10 m. Consequently, the experimental results establish that the spatial path following control method is feasible and that the airship can track a mission path with satisfactory precision.

6. Conclusion

Based on the GBPF principle and the TLC theory, a planar and spatial path following control method for an autonomous airship is presented in this report. In this method, the GBPF principle is utilised to generate the desired attitude and the TLC theory is applied to track the desired attitude promptly. The method is performed in a cascaded structure, including a guidance loop and two TLC procedures. Each TLC procedure is designed in the same format: a pseudo-inversion and a stabilising controller.

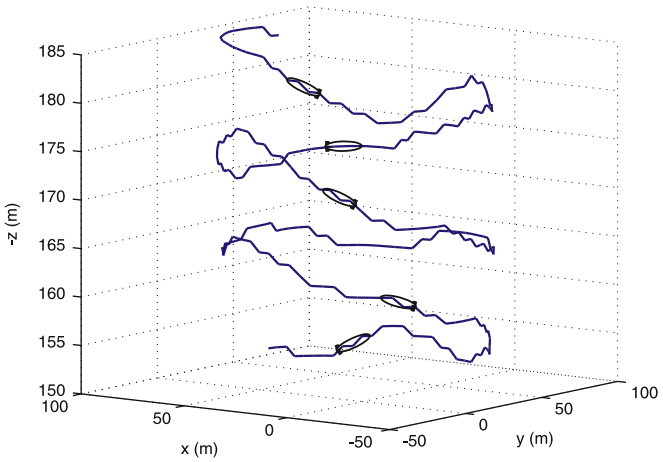

Fig. 20. Spatial position of helix path following experiment.

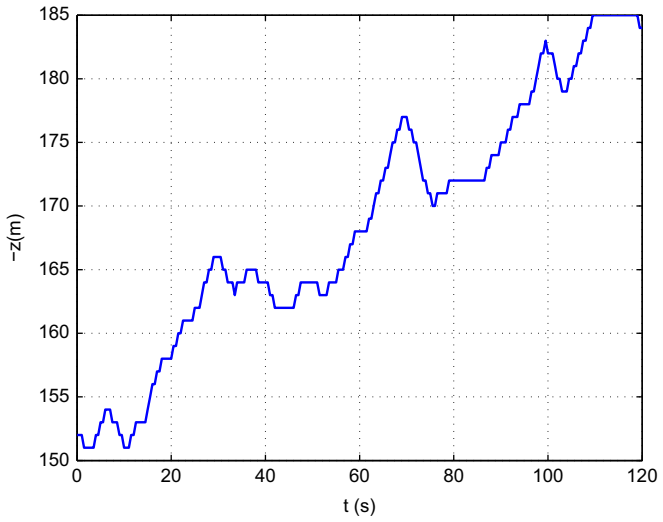

Fig. 21. Altitude of helix path following experiment.

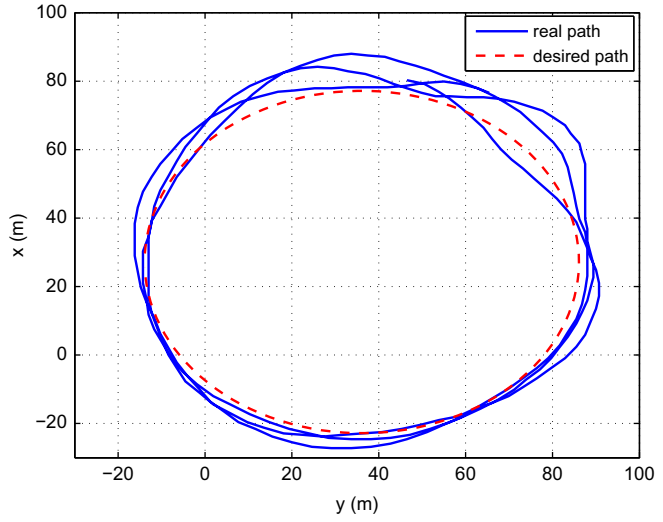

Fig. 22. Planar position of helix path following experiment.

Compared to the traditional gain-scheduling flight control method, whose controller parameters vary with flight modes, the proposed path following control method can operate over the entire desired path without any controller parameter transitions required between different flight modes. The desired path renders all regularly parameterised paths feasible without any singularity point. Furthermore,

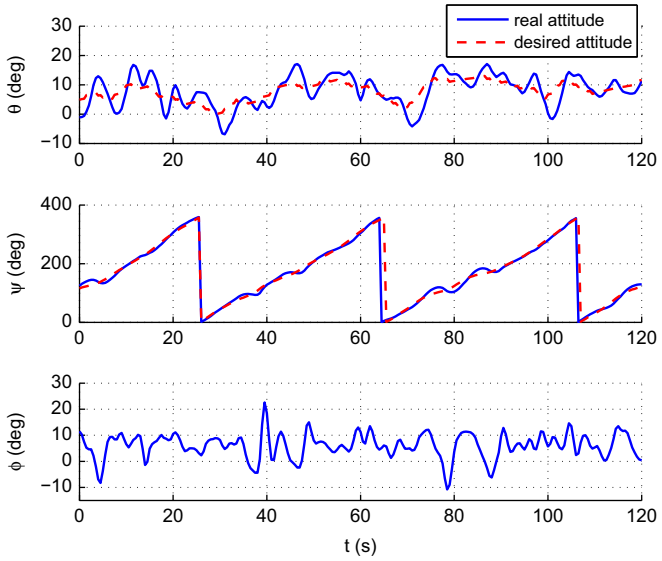

Fig. 23. Attitude of helix path following experiment.

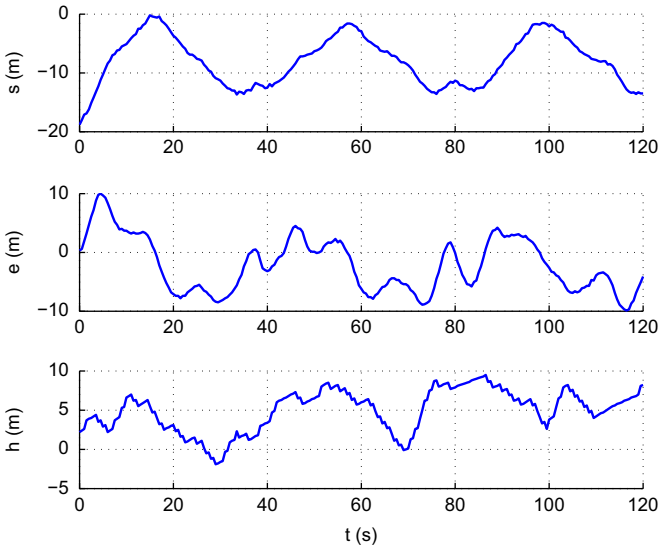

Fig. 24. Tracking error of helix path following experiment.

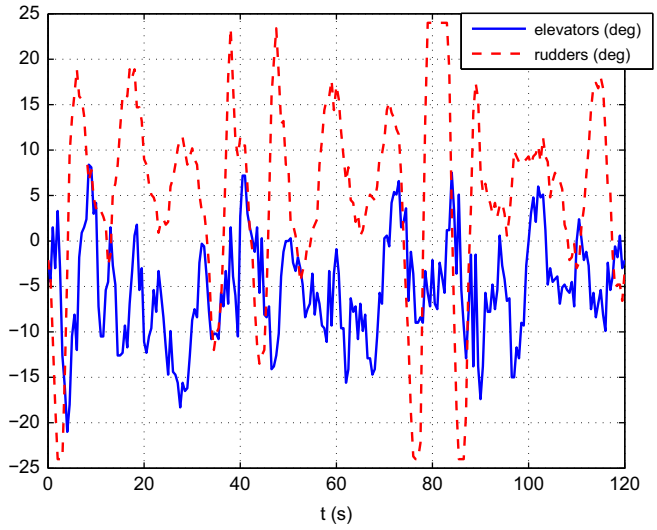

Fig. 25. Control variable of helix path following experiment.

the closed-loop system controlled by this method is proved to be asymptotically stable and its robustness for modelling uncertainties and external perturbations is verified by practical flight experiments. Under this control method, the airship can directly accomplish applications such as surveillance, monitoring, and inspection exploration. Moreover, it should be noted that although the path following control method is designed for airships, it is also suitable for other aircrafts. Additionally, other methods might be able to provide the same performance for the airship, such as LPV or sliding mode control.

Further work includes robust analysis for modelling uncertainties, actuator saturations and external perturbations. In addition, because the aerodynamic surfaces are ineffective at low velocity, the designed path following method does not fit the hovering control of the airship. Therefore, considering some other potential requirements, the hovering control of the autonomous airship in an uncertain wind field will be studied.

Acknowledgments

This study was supported by the National Natural Science Foundation of China under Grant no. 61074010. The authors would like to thank Mr. Liang Sun and Mr. Zhiguang Shi of the Seventh Research Division for their helpful contributions to the flight experiments. In addition, the authors would like to thank Chief Engineer Song Wang and the airship flight team of Beijing Lonsan United Aviation Technology Company for their excellent and professional technical support.

References

Acosta, D. M., & Joshi, S. S. (2007). Adaptive nonlinear dynamic inversion control of an autonomous airship for the exploration of Titan. In *Proceedings of AIAA guidance, navigation and control conference* (pp. 1–13). South Carolina, USA.

Altafini, C. (2002). Following a path of varying curvature as an output regulation problem. *IEEE Transactions on Automatic Control*, *47*(9), 1551–1555.

Azinheira, J. R., & Moutinho, A. (2008). Hover control of an UAV with backstepping design including input saturations. *IEEE Transactions on Control Systems Technology*, *16*(3), 517–526.

Azinheira, J. R., Moutinho, A., & Paiva, E. C. (2009). A backstepping controller for path-tracking of an underactuated autonomous airship. *International Journal of Robust and Nonlinear Control*, *19*, 418–441.

Azinheira, J. R., Paiva, E. C., Ramos, J. G., & Bueno, S. S. (2000). Mission path following for an autonomous unmanned airship. In *Proceedings of the 2000 IEEE international conference on robotics and automation* (pp. 1269–1275). San Francisco, USA.

Bennaceur, S., & Azouz, N. (2012). Contribution of the added masses in the dynamic modeling of flexible airships. *Nonlinear Dynamics*, 67, 215–226.

Bi, F. Y., Wei, Y. J., Zhang, J. Z., & Cao, W. (2010). Position-tracking control of underactuated autonomous underwater vehicles in the presence of unknown ocean currents. *IET Control Theory and Applications*, *4*(11), 2369–2380.

Bijker, J., & Steyn, W. (2008). Kalman filter configurations for a low-cost loosely integrated inertial navigation system on an airship. *Control Engineering Practice*, *16*, 1509–1518.

Breivik, M., & Fossen, T. I. (2004). Path following for marine surface vessels. In *Proceedings of the MTS/IEEE oceans conference* (pp. 2282–2289). Kobe, Japan.

Breivik, M., & Fossen, T. I. (2005a). Guidance-based path following for autonomous underwater vehicles. In *Proceedings of the MTS/IEEE oceans conference* (pp. 2807–2814). Washington DC, USA.

Breivik, M., & Fossen, T. I. (2005b). Principles of guidance-based path following in 2D and 3D. In *Proceedings of the 44th IEEE conference on decision & control, and the European control conference* (pp. 627–634). Seville, Spain.

Frye, M. T., Gammon, S. M., & Qian, C. J. (2007). The 6-DOF dynamic model and simulation of the Tri-Turbofan remote controlled airship. In *Proceedings of the American control conference* (pp. 816–821). New York, USA.

Hovakimyan, N., Lavretsky, E., & Cao, C. Y. (2008). Adaptive dynamic inversion via time-scale separation. *IEEE Transactions on Neural Networks*, *19*(10), 1702–1711.

Huang, R., Liu, Y., & Zhu, J. J. (2009). Guidance, navigation and control system design for tripropeller vertical-takeoff-and-landing unmanned air vehicle. *Journal of Aircraft*, *46*(6), 1837–1856.

Hygounenc, E., & Soueres, P. (2002). Automatic airship control involving backstepping techniques. In *IEEE international conference on systems, man and cybernetics* (pp. 1–6). Toulouse, France.

Jamison, L., Sommer, G.S., & Porche, L.R. (2005). *High-altitude airships for the future force army*. Technical Report of RAND Corporation.

Khalil, H. K. (2002). *Nonlinear systems* (3rd ed.). Pearson Education.

Khoury, G. H., & Gillett, J. D. (1999). *Airship technology* (1st ed.). Cambridge University Press.

Lee, Y. G., Kim, D. M., & Yeom, C. H. (2006). Development of Korean high altitude platform systems. *International Journal of Wireless Information Networks*, *13*, 31–42.

Lee, S. J., Lee, H. C., Won, D. Y., & Bang, H. (2007). Backstepping approach of trajectory tracking control for the mid-altitude unmanned airship. In *Proceedings of AIAA guidance, navigation and control conference* (pp. 1–14). South Carolina, USA.

Lee M., Smith S., & Androulakakis, S. (2009). The high altitude lighter than air airship efforts at the US army space and missile defense command/army forces strategic command. In *18th AIAA lighter-than-air systems technology conference* (pp. 1–26). Seattle, USA.

Liu, Y., & Zhu, J. J. (2007a). Regular perturbation analysis for trajectory linearization control. In *Proceedings of the American control conference* (pp. 3053–3058). New York, USA.

Liu, Y., & Zhu, J. J. (2007b). Singular perturbation analysis for trajectory linearization control. In *Proceedings of the American control conference* (pp. 3047–3052). New York, USA.

Liu, Y., Zhu, J. J., Williams, R. L., & Wu, J. H. (2008). Omni-directional mobile robot controller based on trajectory linearization. *Robotics Autonomous Systems*, *56*, 461–479.

Lonsan (2012). 〈www.lonsan.com.cn/Products_1.asp?oneclass=5&pid=13〉.

Mickle, M. C., Huang, R., & Zhu, J. J. (2004). Unstable, nonminimum phase, nonlinear tracking by trajectory linearization control. In *Proceedings of the 2004 IEEE international conference on control applications* (pp. 812–818). Taipei, Taiwan.

Miller, C. J., Sullivan, J., & McDonald, S. (2007). High altitude airship simulation control and low altitude flight demonstration. In *AIAA infotech@aerospace 2007 conference and exhibit* (pp. 1–22). California, USA.

Moutinho, A., & Azinheira, J.R. (2004). Stability and robustness analysis of the AURORA airship control system using dynamic inversion. In *Proceedings of IEEE international conference on robotics and automation* (pp. 2265–2270). Barcelona, Spain.

Mueller, J. B., & Paluszek, M. A. (2004). Development of an aerodynamic model and control law design for a high altitude airship. In: *AIAA 3rd unmanned unlimited technical conference* (pp. 1–17). Chicago, USA.

Naidu, D. S., & Calise, A. J. (2001). Singular perturbations and time scales in guidance and control of aerospace systems: A survey. *Journal of Guidance, Control and Dynamics*, *24*(6), 1057–1078.

Samson, C. (1995). Control of chained systems: Application to path following and time-varying point-stabilization of mobile robots. *IEEE Transactions on Automatic Control*, *40*(1), 64–71.

Schmidt, D. K. (2007). Modeling and near-space stationkeeping control of a large high-altitude airship. *Journal of Guidance, Control and Dynamics*, *30*(2), 540–547.

Schumacher, C., & Khargonekar, P. P. (1998). Stability analysis of a missile control system with dynamic inversion controller. *Journal of Guidance, Control and Dynamics*, *21*(3), 508–515.

Skjetne, R., & Fossen, T. I. (2001). Nolinear maneuvering and control of ships. In *Proceedings of the MTS/IEEE oceans conference* (pp. 1808–1815). Honolulu, USA.

Smith, M. S., & Rainwater, E. L. (2003). Applications of scientific ballooning technology to high altitude airships. In *AIAA's 3rd annual aviation technology, integration, and operations technical forum* (pp. 1–8). Denver, USA.

Vasconcelos, J. F., Silvestre, C., Oliveira, P., & Guerreiro, B. (2010). Embedded UAV model and LASER aiding techniques for inertial navigation systems. *Control Engineering Practice*, *18*(3), 262–278.

Waishek, J., Dogan, A., & Bestaoui, Y. (2009). Investigation into the time varying mass effect on airship dynamics response. In *47th AIAA aerospace sciences meeting including the new horizons forum and aerospace exposition* (pp. 1–19). Orlando, USA.

Waishek, J., Kumar, V., Dogan, A., & Bestaoui, Y. (2009). Investigation into the time varying mass effect on airship controller performance. In *AIAA atmospheric flight mechanics conference* (pp. 1–12). Chicago, USA.

Xie, S. R., Luo, J., Rao, J. J., & Gong, Z. B. (2007). Computer vision-based navigation and predefined track following control of a small robotic airship. *Acta Automatica Sinica*, *33*(3), 286–291.

Xsens. (2012). 〈www.xsens.com/en/general/mti-g〉.

Yoshikazu, I., Katsuya, S., & Kouichi, S. (2003). Flight control testing for the development of stratospheric platform airships. In *AIAA's 3rd annual aviation technology, integration, and operations technical forum* (pp. 1–11). Denver, USA.

Zhang, Y., Qu, W. D., & Xi, Y.Gg. (2008). Adaptive stabilization and trajectory tracking of airship with neutral buoyancy. *Acta Automatica Sinica*, *34*(11), 1437–1441.

Zheng, Z.W., Zhu, M., & Jiang, G.T. (2009). Flight control software design for stratospheric aerostat. In *International conference on computational intelligence and software Engineering* (pp. 1–5). Wuhan, China: IEEE.

Zhu, J. J. (1995). A unified spectral theory for linear time-varying systems-progress and challenges. In *Proceedings of the 34th IEEE conference on decision & control* (pp. 2540–2546). New Orleans, USA.

Zhu, J. J. (1997). PD-spectral theory for multivariable linear time-varying systems. In *Proceedings of the 36th IEEE conference on decision & control* (pp. 3908–3913). San Diego, USA.

Zhu, B., & Huo, W. (2010). Trajectory linearization control for a quadrotor helicopter. In *8th IEEE international conference on control and automation* (pp. 34–39). Xiamen, China.

Zhu, J. J., Lawrence, D. A., & Fisher, J. (2002). Direct fault tolerant RLV attitude control—A singular perturbation approach. In *Proceedings of AIAA guidance, navigation and control conference* (pp. 1–11). Monterey, USA.